



HELSINKI UNIVERSITY OF TECHNOLOGY
Department of Radio Science and Engineering

Florian Dupuy

**WIDEBAND CHANNEL CHARACTERIZATION:
SIMULATION AND MEASUREMENTS ANALYSIS**

Thesis submitted in partial fulfillment for the degree of Master of Science
in Espoo . . . 2008

Supervisor Professor (Pro tem) Clemens Icheln

Instructor D.Sc. Yves Lostanlen

HELSINKI UNIVERSITY OF TECHNOLOGY

Abstract of the Master's Thesis

Author:	Florian Dupuy
Name of the Thesis:	Wideband Channel Characterization: Simulation and Measurements Analysis
Date:	August 14, 2008
Number of pages:	61
Department:	Department of Radio Science and Engineering
Supervisor:	Prof. (Pro tem) Clemens Icheln
Instructor:	D.Sc. Yves Lostanlen
Abstract:	<p>The development of wireless telecommunication requires higher speed data rates. Wideband MIMO systems are a possible answer to that need. Both wideband and MIMO characteristics enhance multipath propagation, and require a precise knowledge of the channel to properly exploit their capabilities. The extraction of the channel parameters can be done from the measurements, but also from simulations.</p> <p>In the frame of this thesis, the possibility to use ray tracing to derive capacity coverage prediction is studied, based on the comparison with measurements. First the radio channel models are discussed, from the MIMO channel model to the ray tracing methods. Then the measurements methods and the algorithms extracting the channel parameters are presented, before focusing on a measurement campaign to compare prediction from ray tracing and measurements-based SAGE algorithm. Key parameters for capacity –delay spread and angular spread– were first compared, then capacity itself is introduced and a capacity comparison is conducted. Polarization influence on capacity is also studied, and different methods of emulating polarization on ray tracing are studied. Last but not least, the desired capacity coverage prediction is achieved on a wide area around the measurement streets.</p> <p>The simulation results with the ray tracing software are promising. The multipath components were predicted well enough by ray tracing to compute capacity. Then the polarization emulating methods gave interesting results: polarization influences capacity, and the derived capacity values were close enough to those computed from measurement to launch a capacity coverage calculation, first step toward a cellular planning based on MIMO capacity. However, some uncertainties are still left, due to computation time and models approximations.</p>
Keywords:	ray tracing, SAGE, beamforming, radio channel modelling, MIMO, polarization, XPR, capacity

Preface

The work of this thesis has been carried out in the Radio Laboratory of the SMARAD Center of Excellence of the Helsinki University of Technology (TKK) and in SIRADEL SAS in Rennes, France, as a cooperative project between these two entities. I would like to thank both the Radio Laboratory and Siradel R&D for the great possibility to carry out this interesting work. I am very grateful to all my colleagues in both laboratories for giving me a helping hand, or at least cheering me up, in numerous issues.

I want to thank my instructor Dr. Yves Lostanlen, my supervisor Prof. Clemens Icheln, together with Prof. Pertti Vainikainen, for providing facilities and guidance. Thanks also to Dr. Katsuyuki Haneda, Dr. Thierry Tenoux, Veli-Matti Kolmonen and Yoann Corre for the helpful comments and answers, and to Jari Holopainen and Jarkko Viitanen for the nice C321 atmosphere.

My thanks go as well to my friends in Finland, especially Kaisa Korhonen, Juho Mooses Paaso, Olli Pekka Pyysalo and Lorenzo Pansana for the MF-coffee breaks, Viet-Anh Le and Renaud-Alexandre Pitaval, Salva Garrigas, Mélusine Hucault, André Schumacher and Tino Rizzo, for their help, support, good humour and invitations.

Last but not least, I would like to thank my mother and father, together with my sister and brother for their advices, understanding and love.

Otaniemi, August 14, 2008

Florian Dupuy

Table of contents

Abbreviations	5
List of Symbols	6
I – Introduction	9
II – Channel modeling	10
II – 1. Propagation basics	10
II – 2. Propagation models	13
III – Channel sounding	18
III – 1. Measurement methods	18
III – 2. Data extracting algorithms	22
III – 3. Measured parameters and representations	27
IV – Measurements and results	32
IV – 1. Environment, sounder characteristics and parameters of algorithms	32
IV – 2. Comparisons between SAGE and Ray Tracing	36
V – Application: capacity coverage	40
V-1 MIMO capacity	40
V-2 Coverage planning	43
VI – Conclusion	56
Annex A: Polarization influence on capacity	57
References	59

Abbreviations

3G	Third Generation of mobile phone standards and technology
3GPP	Third Generation Partnership Project
4G	Fourth Generation of mobile phone standards and technology
AGC	Automatic Gain Control
BF	Beamforming
CDF	Cumulative (or probability) Distribution Function
CIR	Channel Impulse Response
COST	European Cooperation in the Field of Scientific and Technical Research
DoA	Direction of Arrival
DoD	Direction of Departure
DTM	Digital Terrain Model
ESPRIT	Estimation of Signal Parameter Via Rotational Invariance Techniques
FMC	Fixed Mobile Convergence
GO	Geometrical Optics
HSDPA	High-Speed Downlink Packet Access
ISIS	Initialization and Search Improved SAGE
LOS	Line of Sight
MEBAT	Measurement-Based Antenna Test Bed
MIMO	Multiple-Input-Multiple-Output
MUSIC	Multiple Signal Classification
NLOS	Non Line of Sight
PDP	Power Delay Profile
PN	Pseudorandom Noise
rms	Root Mean Squared
RT	Ray Tracing
Rx	Receiver
SAGE	Space-Alternating Generalized Expectation-maximization
SIMO	Single-Input-Multiple-Output
SISO	Single-Input-Single-Output
SNR	Signal-to-Noise Ratio
TKK	Teknillinen Korkeakoulu (Helsinki University of Technology)
Tx	Transmitter
UTD	Uniform Theory of Diffraction
WINNER	Wireless World Initiative New Radio
XPR	Cross-Polarization Ratio

List of Symbols

$a(h_m)$	mobile station antenna height correction
α_i	Doppler shift on path i
α_{Fr}	Frobenius normalization factor
α_{det}	weighing coefficient for the deterministic attenuation
$\mathbf{b}_{Rx,i,l}, \mathbf{b}_{Tx,i,k}$	single antenna responses for Rx and Tx containing both polarizations
$c(t)$	PN code
c_0	speed of light
$\mathbf{C}(\varphi, \theta)$	Rx steering vector in the direction (φ, θ)
$C_{free\ space}$	free space correction
\mathcal{C}	ergodic channel capacity
$\mathcal{C}_{q\%outage}$	$q\%$ outage channel capacity
d	distance between base and mobile stations
E_i	complex amplitude of path i
f_0, f_{LO}	carrier frequency
$\varphi_{Rx,i}, \varphi_{Tx,i}$	azimuth angle of arrival and departure of i^{th} path
$\bar{\varphi}$	“mean” azimuth angle
ϕ_{spread}	rms azimuth angular spread
Φ	covariance matrix of the transmitted signal \mathbf{x}
$g_{Rx,i,l}$	impulse response of l^{th} Rx in the DoA of ray i
$g_{Tx,i,k}$	impulse response of k^{th} Tx in the DoD of ray i
G_R, G_T	receiving and transmitting antenna gain
$h(\tau, t)$	channel impulse response
h_b, h_m	base station and mobile station antenna height
\mathbf{H}	channel matrix
$\tilde{\mathbf{H}}$	normalized channel matrix
$\mathcal{H}(Y)$	entropy of random variable Y
$\mathcal{H}(Y X)$	conditional entropy of Y given X
$\mathcal{I}(X;Y)$	mutual information between random variables X and Y
γ	dilatation factor
γ_i	complex path weight of ray i

Γ_i	matrix of the complex path weights for each polarization combination
l_i	electrical length of ray path i
L	number of Rx antennas
L_c	length of the code
$L_{deterministic}$	deterministic attenuation
$L_{free\ space}$	free space loss
L_p, L_{path}	pathloss
λ	wavelength of the radio wave
Λ	loglikelihood function
M	number of paths
\mathbf{n}	background noise vector
N	number of Tx antennas
\mathbf{N}_s	noise part (beamforming)
p_n	noise power (related to $\mathbf{w}_c^H \cdot \mathbf{n}(t)$)
p_s	power of the ray in the look direction
P_0	maximum total transmitting power
P_R, P_T	received and transmitted power
P_y	mean power of the output
$P_{VV}, P_{VH}, P_{HV}, P_{HH}$	polarization powers
r	signal received
$R_c(\tau)$	autocorrelation function of $c(t)$
\mathbf{R}	correlation matrix of $\mathbf{y}(t)$
\mathbf{R}_s	correlation matrix of $\mathbf{N}_s(t)$
ρ	average SNR at each receiver branch
s	signal sent
σ_n^2	noise power
t	time
T_C	period of a chip code
τ_i	time delay of arrival of i^{th} path
$\bar{\tau}$	mean delay
$\tau_{rms\ spread}$	rms delay spread
$\theta_{Rx,i}, \theta_{Tx,i}$	elevation angle of arrival and departure of i^{th} path

$\underline{\theta}_i$	set of parameters associated with i^{th} ray
w_k, \mathbf{w}	beamforming weights
x_k	signal at the k^{th} Tx antenna
\mathbf{x}	vector of x_k Tx signals
\hat{x}_s	signal from s^{th} ray path arriving at the Rx
XPR_V, XPR_H	vertical and horizontal cross-polarization ratios
y	output signal
\mathbf{y}	signal induced by <i>all</i> Tx antennas on <i>all</i> Rx antennas through <i>all</i> rays
\mathbf{y}_i	signal induced by <i>all</i> Tx antennas on <i>all</i> Rx antennas through i^{th} ray
$\mathbf{y}_{i,k}$	signal induced by k^{th} Tx antenna on <i>all</i> Rx antennas through i^{th} ray
$y_{i,k,l}$	signal induced by k^{th} Tx antenna on the l^{th} Rx antenna through i^{th} ray

I – Introduction

Currently we are witnessing a fixed-mobile convergence (FMC), which is trying to merge two different technologies: fixed network and mobile network. Fixed networks are offering very high data rates (100 Mb/s, or more, with optic fiber), adapted to multimedia applications such as high-definition video streaming and teleconferencing, whereas mobile networks are much more limited: 3G systems can offer up to 14 Mb/s only (HSDPA provides up to 14.4 Mb/s on the downlink and 5.8 Mb/s on the uplink). Multiple Input Multiple Output (MIMO) systems are a step toward this convergence, by exploiting the spatial dimension of the mobile radio channel: they use several antenna elements and adaptive signal processing, at both transmitter and receiver. This allows deploying several parallel links into different spatial directions at the same time and frequency, offering higher capacity than SISO (Single Input Single Output) or SIMO (Single Input Multiple Output) systems. It is all the more true if the channels between antenna elements are uncorrelated; rich multipath environments are then the most desirable.

Nevertheless, a precise knowledge of the channel is needed to properly exploit MIMO benefits, especially for wideband systems, which are increasing the multipath effect even more. Two sophisticated means are disposable for the characterization of the channel: measurement with a channel sounder, and simulation with a deterministic tool, both providing an estimation of the space-time channel. Measurements are very costly and laborious which explains why extracted data is only scarcely available, hence simulation is of great interest. However, since its reliability has so far been established mainly for pathloss prediction, deterministic tools still have to be used with caution for the prediction of the multipath components, or of more complex parameters such as capacity (which gives a theoretical maximum data rate).

The goal of the present master's thesis is to ascertain the validity of the ray tracing (RT) deterministic method used in the Volcano software of Siradel for predicting MIMO coverage, where coverage is defined as the maximum distance where a given capacity is achieved. To that end a comparison between RT and measurements will be conducted based on parameters influencing capacity, before focusing the comparison on capacity itself. The measurement data analyzed mainly consisted of 5 routes from one single measurement campaign, representing almost 20,000 snapshots, with LOS (Line of Sight) and NLOS (Non-LOS) cases. The present thesis was limited to this environment for computing time reasons, and because of the already huge amount of data collected. Last but not least, relying on the comparison results, a coverage prediction will be achieved for a 1 km² area around the measurement campaign.

This thesis research has required the use of Elektrobit ISIS (Initialization and Search Improved SAGE) algorithm output, of Siradel Volcano ray tracing software, together with FM-Kartta Oy 3D-map of Helsinki, and of TKK MEBAT tool. Numerous tools have also been coded in Matlab for calculation, analysis and comparison of the results.

II – Channel modeling

The first step in deriving coverage is to have a model of the channel. To that end, some propagation basics are necessary; after a quick review of the needed propagation knowledge, the different types of modeling will be introduced.

II – 1. Propagation basics

Signal model: A MIMO signal model will be presented in this part, which will be used later for the description of the data extracting algorithms presented in III – 2. The model should describe the propagation channel as precisely as possible, but at the same time it should be possible to extract its parameters from the finite measurement data.

Consider a MIMO system with L transmitting antenna elements and N receiving antenna elements (Figure 2.1). The signal at the k^{th} Tx (transmitter) antenna is noted $x_k(t)$, while the signal at the l^{th} Rx (Receiver) antenna is denoted $y_l(t)$. The radio waves between the transmitter and the receiver can be modeled as a superposition of discrete rays based on geometric optics (GO) [1, 2, 3]. The more rays are considered, the better the accuracy of the model. Note that the GO approximation implies considering the incident waves as plane waves.

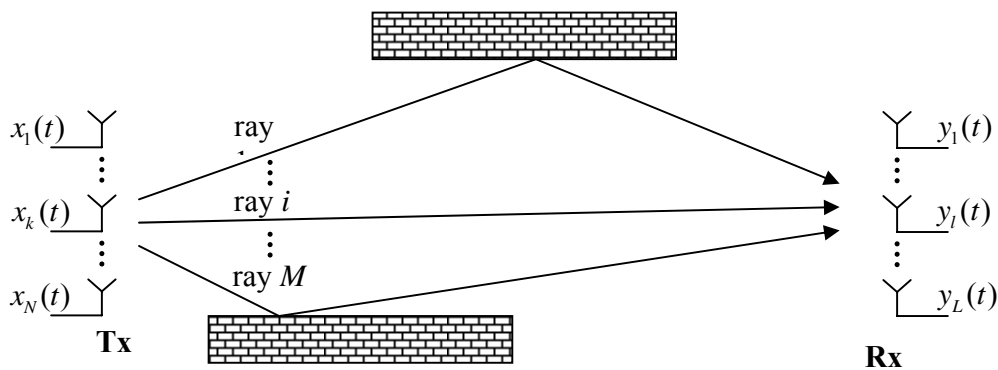


FIG. 2.1: General MIMO channel

A ray is characterized by the azimuth and elevation angles at the Tx (Direction of Departure), the azimuth and elevation angles at the Rx (Direction of Arrival), the time-delay of arrival, and the amplitude, phase and polarization (orientation of the electrical field component) at the receiver. In the present thesis, polarization is defined in reference to the horizontal and vertical directions.

If the SISO system formed by k^{th} Tx antenna and l^{th} Rx antenna is considered, and a signal $x_k(t)$ transmitted over a single ray i at a carrier frequency f_0 , then the received signal $y_{i,k,l}(t)$ is as follow [3]:

$$y_{i,k,l}(t) = \gamma_i \cdot g_{Tx,i,k}(t) * g_{Rx,i,l}(t) * x_k(t - \tau_i) e^{-j2\pi f_0 \tau_i}, \quad (2.1)$$

where $*$ denotes the convolution operator, γ_i is the parameter describing all the frequency independent effects including propagation losses, $\tau_i = l_i/c_0$ is the time taken for the signal to travel from Tx to Rx, l_i being the electrical length of the ray path and c_0 the speed of light, $g_{Tx,i,k}(t)$ is the impulse response of the k^{th} transmitter in the direction of departure $(\varphi_{Tx,i}, \theta_{Tx,i})$ of ray i , $g_{Rx,i,l}(t)$ is the impulse response of the l^{th} receiver in the direction of arrival $(\varphi_{Rx,i}, \theta_{Rx,i})$ of ray i . $\varphi_{Tx,i}$ is the azimuth angle of departure, $\theta_{Tx,i}$ the elevation angle of departure, $\varphi_{Rx,i}$ the azimuth angle of arrival, $\theta_{Rx,i}$ the elevation angle of arrival. The system was supposed to be time-invariant. To take the polarization into account (as γ_i , $g_{Tx,i,k}(t)$ and $g_{Rx,i,l}(t)$ depend on the orientation of the electric field component), and to express the directivity of antennas, complex beam patterns of the Tx and the Rx are introduced, which are defined for both horizontal and vertical polarization [3]:

$$\mathbf{b}_{Tx,i,k} = \begin{bmatrix} b_{Tx,k,H}(\varphi_{Tx,i}, \theta_{Tx,i}) & b_{Tx,k,V}(\varphi_{Tx,i}, \theta_{Tx,i}) \end{bmatrix} \quad (2.2)$$

$$\mathbf{b}_{Rx,i,l} = \begin{bmatrix} b_{Rx,l,H}(\varphi_{Rx,i}, \theta_{Rx,i}) & b_{Rx,l,V}(\varphi_{Rx,i}, \theta_{Rx,i}) \end{bmatrix} \quad (2.3)$$

Note that vectors and matrices are written in bold font; the same notation is thereafter used. The (2.1) SISO model then becomes [3]:

$$y_{i,k,l}(t) = \mathbf{b}_{Rx,i,l} \cdot \mathbf{\Gamma}_i \cdot \mathbf{b}_{Tx,i,k}^T \cdot g_{Tx,k}(t) * g_{Rx,l}(t) * x_k(t - \tau_i) e^{-j2\pi f_0 \tau_i}, \quad (2.4)$$

where $\mathbf{\Gamma}_i$ is the 2 x 2 matrix of the coefficients γ_i for each polarization combination:

$$\mathbf{\Gamma}_i = \begin{bmatrix} \gamma_{HH,i} & \gamma_{VH,i} \\ \gamma_{HV,i} & \gamma_{VV,i} \end{bmatrix} \quad (2.5)$$

The $L \times 1$ matrix $\mathbf{y}_{i,k}(t)$ of the signal induced by the i^{th} ray path on all elements of the receiver antenna is then (SIMO case, one single path):

$$\mathbf{y}_{i,k}(t) = \begin{bmatrix} y_{i,k,1}(t) \\ \dots \\ y_{i,k,L}(t) \end{bmatrix} = e^{-j2\pi f_0 \tau_i} \begin{bmatrix} \mathbf{b}_{Rx,i,1} \cdot \mathbf{\Gamma}_i \cdot \mathbf{b}_{Tx,i,k}^T \cdot g_{Tx,k}(t) * g_{Rx,1}(t) * x_k(t - \tau_i) \\ \dots \\ \mathbf{b}_{Rx,i,L} \cdot \mathbf{\Gamma}_i \cdot \mathbf{b}_{Tx,i,k}^T \cdot g_{Tx,k}(t) * g_{Rx,L}(t) * x_k(t - \tau_i) \end{bmatrix} \quad (2.6)$$

And to get the MIMO system model with one single ray path, the N transmitting antennas have to be taken into account:

$$\mathbf{y}_i(t) = \sum_{k=1}^N \mathbf{y}_{i,k}(t) = \begin{bmatrix} \sum_{k=1}^N y_{i,k,1}(t) \\ \dots \\ \sum_{k=1}^N y_{i,k,L}(t) \end{bmatrix} + \mathbf{n}_i(t) \quad (2.7)$$

Note that the background noise has now been taken into account: $\mathbf{n}_i(t)$ is the $L \times 1$ noise matrix. And, finally, the MIMO system model with M ray paths is obtained by summing the contributions of the different rays:

$$\mathbf{y}(t) = \sum_{i=1}^M \mathbf{y}_i(t) = \begin{bmatrix} \sum_{i=1}^M \sum_{k=1}^N y_{i,k,1}(t) \\ \dots \\ \sum_{i=1}^M \sum_{k=1}^N y_{i,k,L}(t) \end{bmatrix} + \mathbf{n}(t), \quad (2.8)$$

where $\mathbf{n}(t) = \sum_{i=1}^M \mathbf{n}_i(t)$.

This model is valid only if the system is time invariant; if some elements on the path (or Rx/Tx) are moving, then a Doppler shift $\alpha_i = f_0 v_i / c_0$ has to be added for each path [3], where v_i is the speed vectors projection on the propagation path, and then equation (2.1) should be rewritten as

$$y_{i,k,l}(t, \tau) = \gamma_i \cdot g_{Tx,i,k}(t) * g_{Rx,i,l}(t) * x_k(t - \tau_i) e^{-j2\pi f_0(\tau_i + \alpha_i \tau)} \quad (2.9)$$

Propagation mechanics: Propagation of the signal endures losses from free-space propagation losses and from interaction with the obstacles. In the frame of this thesis, only two types of interaction will be considered: reflection and diffraction.

- *Propagation in free space:* In ideal, free-space conditions, propagation is described by Friis equation (e.g. [4]):

$$P_R = P_T G_T G_R \left(\frac{\lambda}{4\pi d} \right)^2, \quad (2.10)$$

where P_T is the transmitted power, G_T the transmitting antenna gain, P_R the received power, G_R the receiving antenna gain, λ the wavelength of the radio wave and d the transmitter-receiver distance.

- *Reflection*: Reflection occurs when the obstacle is large compared to the wavelength. If the surface is smooth enough (irregularities much smaller than the wavelength), then the reflection is commanded by Snell's law (angle of incidence = angle of reflection)
- *Diffraction*: Diffraction occurs on the edges of the obstacles: according to Huygens-Fresnel principle, these edges can be considered as secondary spherical wave sources, thus lighting "shadow" regions. Building vertical edge diffraction and over-rooftop diffraction will be especially considered.

II – 2. Propagation models

To derive coverage there are several types of propagation models, for example statistical, empirical, semi-empirical or deterministic models. Statistical and empirical methods try to reproduce certain channel characteristics observed during measurements. Deterministic models, on the contrary, attempt to simulate the physical wave propagation process.

Empirical and statistical models: The amplitude of the received signal is usually modelled as the product of three main empirical methods are COST-Hata (or Okumura-Hata), COST231-Walfish-Ikegami and Walfish-Bertoni methods. All these methods provide only pathloss variation; hence the derived coverage is based upon pathloss only. Nonetheless, statistical channel models can complete this information by providing slow fading information and small-scale fading with space-time information. The most used models are COST 273 MIMO channel model [5], 3GPP Spatial Channel Model (SCM) [6] and WINNER channel model [7]. For instance COST 273 channel model provide shadow fading, delay spread and angular spreads as correlated log-normal random variables (but also power delay profile distribution, azimuth/elevation power spectrum distribution, ...) [5]. The multipath components are nonetheless not known but chosen randomly from the appropriate probability distribution.

The COST-Hata model is based on measurements done in 1968 in Tokyo by Okumura. The closed form expression has been submitted by Hata in 1980 [8], before being extended by the action 231 of the European Cooperation in the Field of Scientific and Technical Research (COST) [9]:

$$L_p = A + B \log_{10} f_0 - 13.82 \log_{10} h_b - a(h_m) + (C - 6.55 \log_{10} h_b) \log_{10} d \quad (2.11)$$

where L_p is the pathloss, A , B and C are constants, f_0 is the carrier frequency, h_b the base station antenna height, h_m the mobile station antenna height, d the distance between base and mobile stations, and $a(h_m)$ the mobile station antenna height correction (which is derived differently according to the either dense city, city, suburban or rural area environment, more details can be found in [8]). The model is limited by the original measurement spatial resolution (20 meters), and has been designed for frequencies from 150 to 2000 MHz.

The COST231-Walfish-Ikegami pathloss model, which has been introduced in 1991 [9, 10], distinguishes two cases for pathloss prediction: Line of Sight (LOS) and Non Line of Sight (NLOS). As for the Walfish-Bertoni model [11], it also introduces a better recognition of knife-edges between transmitter and receiver than COST-Hata model, and is thus better suited for urban areas.

Deterministic modeling (ray-tracing): Deterministic modeling, which gives results more precise than the previous methods, can provide space-time information, and hence allows an analysis of the obtained data.

A deterministic prediction requires the use of suitable formulations of the physical wave propagation phenomena. Geometrical Optics (GO) is usually used together with Uniform Theory of Diffraction (UTD) [12]. GO supposes that the dimensions of the objects encountered are big in comparison with the wavelength, which thus leads to the use of ray-optical methods, while UTD is extending the GO by adding diffraction geometrical modeling. This ray-approach modeling is thus called ray tracing. The propagation environment (objects present in the experiment) has to be described, generally by the use of raster or vectors. This point is delicate, as many questions arise, as the precision required (vertical and horizontal), the objects needed to be taken into account (balconies, lampposts, traffic...), the parameters (position, speed, type of material). And, naturally, the more details the geographical map contains, the more expensive it is.

Several ray tracing methods have been developed in the past 15 years for different propagation environment. Nonetheless, the present thesis focuses on the method used by Siradel's Volcano software [13, 14]. The method is based on a mixed 2D-3D ray launching method [15]. It consists of 3 steps:

Direct path contribution: The direct path contribution is simply computed by analyzing the straight-line path between transmitter and receiver. The pathloss between the receiver and the transmitter is obtained by adding free space loss to the free space corrections and the computed deterministic losses:

$$L_{path} \text{ (dB)} = L_{free \ space} + C_{free \ space} + \alpha_{det} L_{deterministic} \quad (2.12)$$

where L_{path} is the pathloss, $L_{free \ space}$ the free space loss, $C_{free \ space}$ the free space correction, $L_{deterministic}$ the deterministic attenuation, and α_{det} the weighing coefficient for the deterministic attenuation. $L_{deterministic}$ represents the losses due to the interactions with the environment (e.g. diffractions and reflections), which are weighed by a tuning constant α derived in the calibration process. $L_{free \ space}$ and $C_{free \ space}$ are given by:

$$L_{free \ space} = -27.56 + 20 \log_{10}(f_0) + 20 \log_{10}(d) \quad (2.13)$$

$$C_{free \ space} = A_C + (B_C - 20) \log_{10}(d) \quad (2.14)$$

where d is the path length in meters, and f_0 the frequency in MHz. A_C and B_C are constants, whose values are different for LOS and NLOS paths, and they are generally defined through calibration. $L_{free \ space}$ corresponds to the losses if there were no obstacles between the transmitter and the receiver, whereas $C_{free \ space}$ takes into account the environment in a statistical way, similarly to the previous COST models. An enhanced version of Deygout method [16] is also used to take into account diffraction over rooftops, impacting $L_{deterministic}$ in the budget link.

2D ray launching: One speaks of *ray launching* when, in a first place, tracing the rays is done disregarding the receiver location, that is, rays are launched in every direction with a given angular step. Ray tracing, on the contrary, only derives the ray paths from Tx to Rx, therefore ray launching output contains more results ray tracing and is thus especially adapted for coverage prediction. In the software used, rays are launched from the transmitter to each wall at a given maximal distance, with given maximum angular and distance separations (i.e. distance on the wall), and reflection on the wall is computed (Figure 2.2, green beam of rays). The same is done for diffractions on the building edges (Figure 2.2, blue ray).

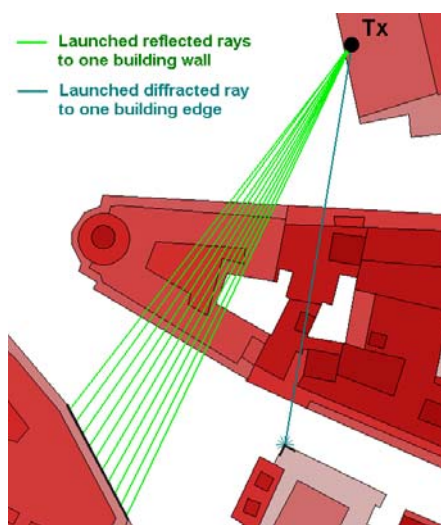


FIG. 2.2: Ray launching

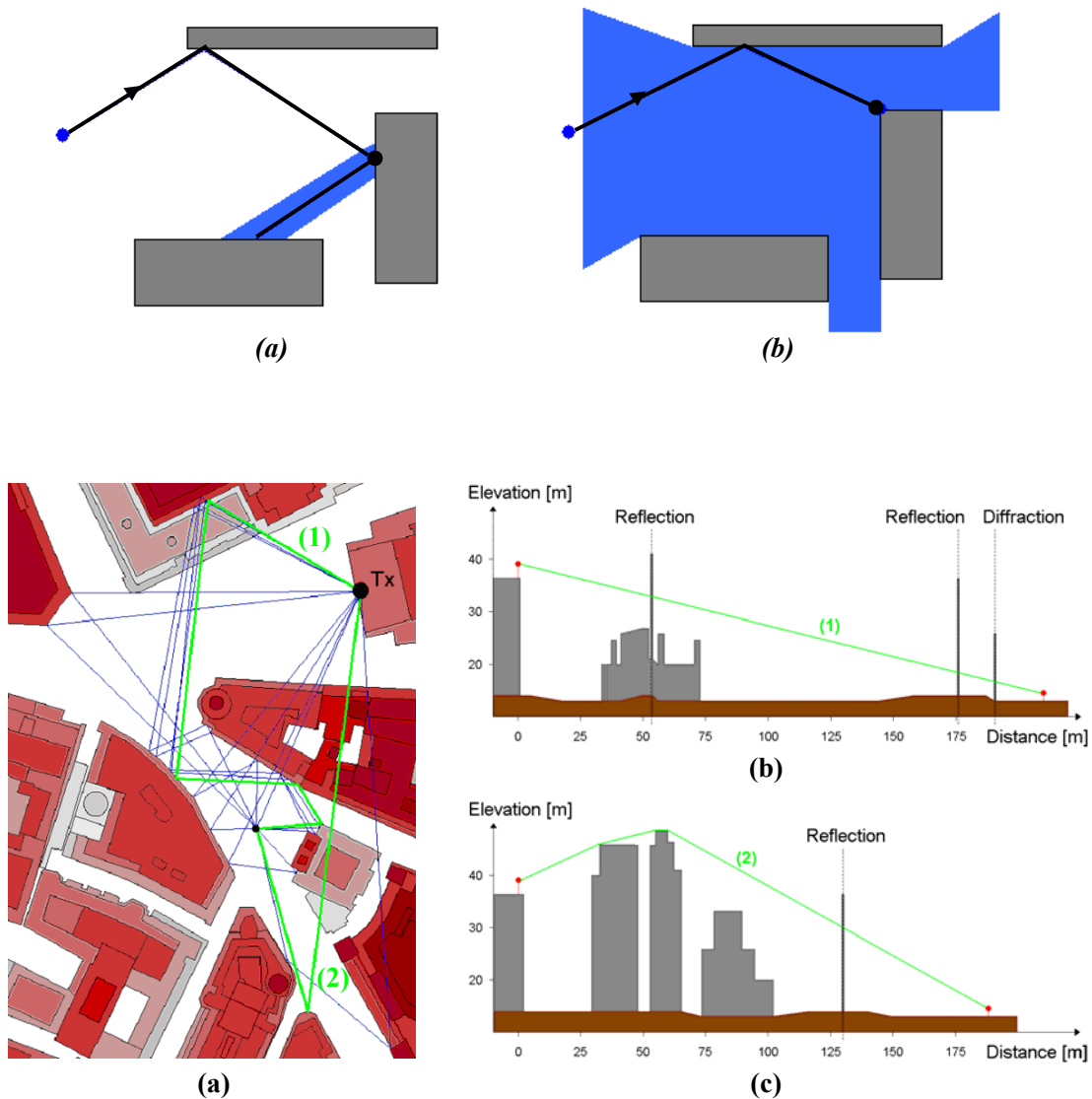


FIG. 2.4 Examples of 2D ray paths and unfolded 3D paths

Each ray then contained a *visibility mask* which is its covered surface (Figure 2.3). This visibility mask is limited by given maximum numbers of reflections and diffractions, by the beamwidth of the ray and by building obstructions. For instance in Figure 2.3a, the visibility mask for the reflection occurring on the point on the right is a zone with a given width centered on the reflected ray (derived by GO); in Figure 2.3b, the visibility mask for the diffraction occurring on the building edge on the right is only obstructed by buildings, as the ray can be diffracted in any direction. Once the ray launching has been done, the algorithm looks for receivers in the visibility masks.

3D ray path and path contribution: As soon as a receiver is found to be in the mentioned zone, the path is examined in the vertical plane; e.g. in Figure 2.4a the path (1) is seen as in Figure 2.4b once “unfolded”, and path (2) as in Figure 2.4c. All vertical profiles of the path between two interactions are just put end to end to get the complete “2.5D” vertical profile. Then the vertical path of the ray is computed by taking the shortest path between

the transmitter and the receiver on the aforementioned profile. For instance, it corresponds in Figure 2.4b to a straight line between Tx and Rx. The validity of the ray can then be checked; for instance, if the building on the top of Figure 2.4a, on which the ray (1) reflects, was below the green straight line in Figure 2.4b, the path would be invalid: the first reflection would not take place, thus this path could not exist.

The power contribution of the ray processed is then derived with the help of an enhanced Deygout method for the diffraction over rooftops (vertical plane), with UTD for the interactions on the horizontal plane. The link budget in (2.12) can be used, if considering that $L_{deterministic}$ now takes into account both UTD and Deygout method. The other multipath components (among others, departure and arrival angles and delay) are added to the ray spectrum of the receiver.

The flowchart of the algorithm is summarized in Figure 2.5.

The method of the tool used has been presented and now channel data can be analyzed and pathloss coverage provided. The validity of the parameters provided needs to be checked with measurement results. How to measure the channel and derive the channel data would be presented in the next chapter.

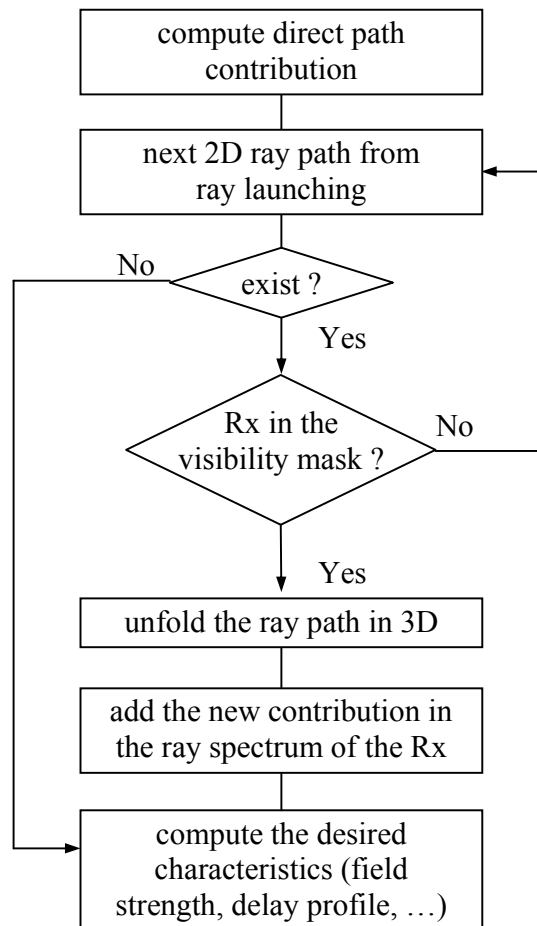


FIG. 2.5: Flowchart of Volcano 3D ray tracing

III – Channel sounding

The goal of a channel sounder is to characterize the channel, by analyzing at the receiver the channel response to a signal sent from the transmitter. Different wideband measurements methods are here presented, deriving the channel impulse response, before introducing the data extraction algorithms, which takes advantage of the MIMO system to compute the space-time channel matrix, and lastly the data extracted itself.

III – 1. Measurement methods

The three different methods presented in this part [17] (direct pulse, matched filter and sliding correlator measurements) are introduced for SISO wideband transmission. The sequential channel sounding introduced at the end of this section allows using them for a MIMO case.

Direct pulse measurement: This method has been used the first time in 1950 in New York City by Young and Lacy, at a frequency of 450 MHz [18]. An impulse signal is generated at the transmitter, modulated, and its echoes are observed at the receiver [17]. Figure 3.1 presents the measurement system.

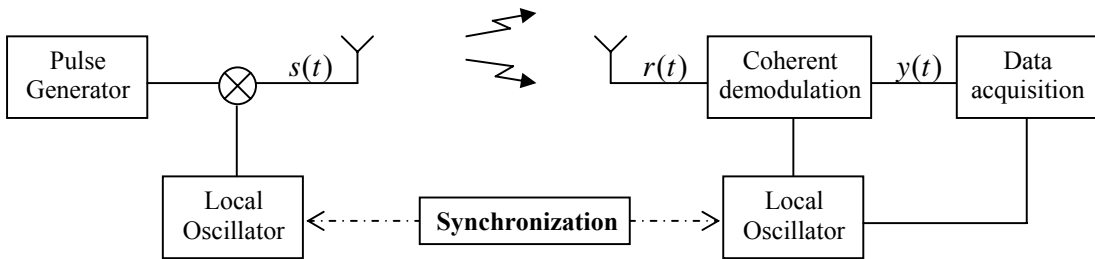


FIG. 3.1: Direct pulse measurement

The signal sent $s(t)$ is a pulse modulated signal, thus:

$$s(t) = \text{rect}_{\Delta t}(t) \cos(2\pi \cdot f_{LO} \cdot t), \quad (3.1)$$

where f_{LO} is the frequency used, and $\text{rect}_{\Delta t}$ the rectangular function of width Δt .

If the channel impulse response is denoted by $h(\tau, t)$, the received signal $r(t)$ can be written as:

$$r(t) = h(\tau, t) * s(t), \quad (3.2)$$

where $*$ is the convolution operator. After coherent demodulation, the signal $r(t)$ becomes:

$$y(t) = \frac{1}{2} h(t) * \text{rect}_{\Delta t}(t) \quad (3.3)$$

Matched filter measurement: To improve the SNR (Signal to Noise Ratio), matched filtering can be used, in association with a transmitted pseudorandom noise (PN) signal of maximal length [17, 19]. The system considered is then in Figure 3.2, and the signal sent is:

$$s(t) = c(t) \cos(2\pi \cdot f_{LO} \cdot t) \quad (3.4)$$

where $c(t)$ is the PN code used (Figure 3.3). The impulse response of the ideal matched filter (assuming white noise) is a time-reversed scaled version of the signal $c(t)$:

$$h_{MF}(t) = \frac{1}{LT_C} c(LT_C - t) \quad (3.5)$$

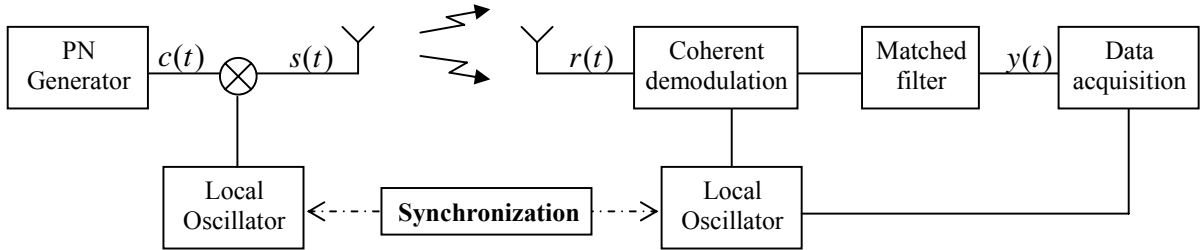


FIG. 3.2: Matched filtering measurement

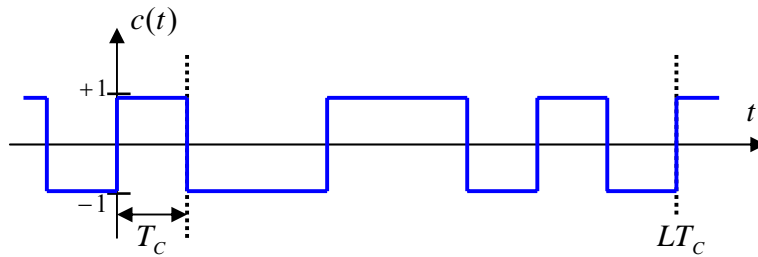


FIG. 3.3: PN code of length L , chip length T_C

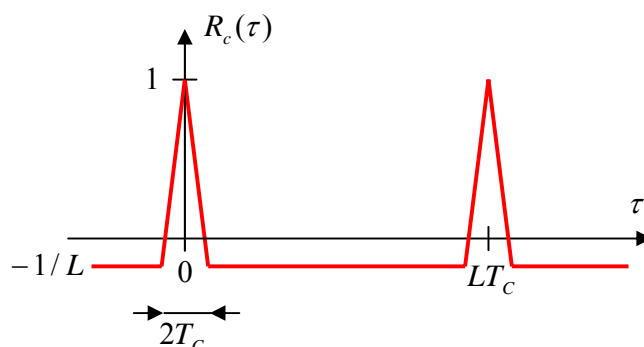


FIG. 3.4: Autocorrelation of a PN code of length L_c
(case of a maximum-length sequence [19])

where L_c is the length of the code and T_c the period of a chip code. Assuming the channel being stationary over $L_c T_c$, one can derive the output signal $y(t)$:

$$y(t) = \frac{1}{2} h(\tau, t) * R_c(\tau) \quad (3.6)$$

where $R_c(\tau)$ is the autocorrelation function of the signal $c(t)$ (Figure 3.4). If the channel impulse response has a maximum length of $L_c T_c$ in the delay domain:

$$h(\tau, t) = 0 \quad \text{for } \tau \notin [0; L_c T_c] \quad (3.7)$$

Then the output signal $y(t)$ can be rewritten as:

$$y(t) = \frac{1}{2} (h * R_{c_0})(t - n L_c T_c, t) \quad \text{for } \tau \in [n L_c T_c; (n+1) L_c T_c] \quad (3.8)$$

where $R_{c_0}(t)$ is the function $R_c(t)$ restricted on $[-L_c T_c / 2; L_c T_c / 2]$

Sliding correlator measurement: This method is also known as Cox correlator, being originally introduced by Donald C. Cox in 1972 [20]. Its principle (Figure 3.5) is to multiply the signal received with a slightly slower or quicker copy of the transmitter PN, and to subsequently apply a low-pass filter [17, 19].

$$f_c' = f_c \pm \Delta f \quad (3.9)$$

where f_c is the frequency of the PN code at the transmitter, and f_c' the frequency of its copy at the receiver. This operation dilates the time of the channel impulse response,

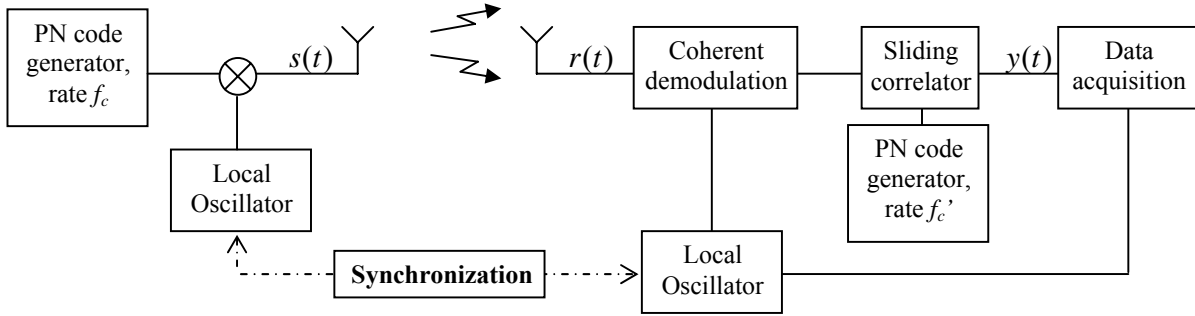


FIG. 3.5: Sliding correlator measurement

therefore reducing the measurement bandwidth and minimizing the hardware requirements. This bandwidth compression is obtained at the cost of measurement time.

The output signal $y(t)$ can also here be derived with the method used in the previous paragraph:

$$y(t) = \frac{1}{2} (h * R_{c0}) \left(\frac{t}{\gamma} - nLT_c, t \right) \quad \text{for } \tau \in [nLT_c; (n+1)LT_c[\quad (3.10)$$

where $\gamma = \frac{f_c}{f_c - f_c'}$ is the dilatation factor. For instance, in [20], $f_c = 10$ MHz, $f_c' = f_c - 2$ kHz, and hence $\gamma = 5000$.

Sequential channel sounding: The acquisition of the MIMO response is done sequentially, thanks to switching sequences at transmitter and receiver, as presented in Figure 3.6 for a 3x3 MIMO channel sounding. Hence, the switching process needs precise synchronization. A rubidium clock is usually used for this purpose. The rubidium clock is also synchronizing the whole system, if no cable is used, as seen in Figures 3.1, 3.2 and 3.5.

A full Tx-Rx switching sequence is called a snapshot. The switching process should be fast enough to fulfill the hypothesis that the channel is invariant over the whole snapshot. Note the guard interval (one blank period, in green on the graph) used to avoid switching transients.

TKK channel sounder: The details of the channel sounder whose results are used in this work [21, 22] are given in Table 3.1.

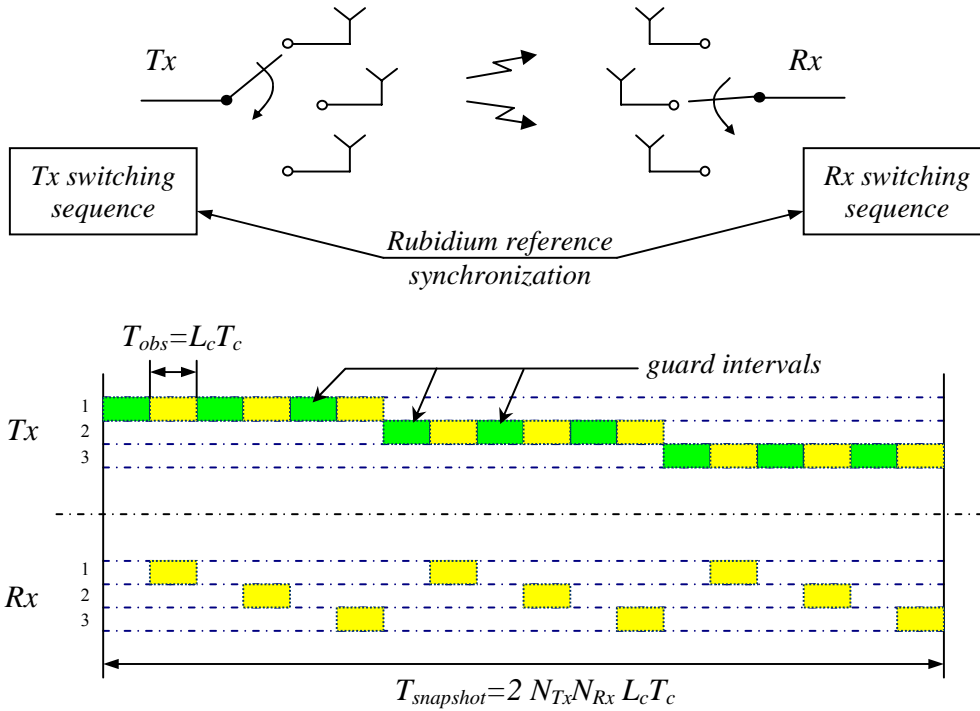


FIG. 3.6: Simplified principle of a sequential 3x3 MIMO channel sounding

TABLE 3.1: TKK channel sounder

Central frequency	5.3 GHz
Measurement method	matched filtering sliding correlator
PN code used	maximum length code length of 255, chip rate of 60 MHz
MIMO system size	30x30
Sequential channel sounding	one snapshot measurement in 8.7 ms

III – 2. Data extracting algorithms

Various algorithms exist to extract the space-time channel characteristics from the channel sounder output. Beamforming is usually described as the simplest and most robust method: it can be seen as Fourier processing, and its simplest form corresponds to pointing the antenna array to a given direction. In contrast to it, the so-called super-resolution algorithms are more sophisticated and more precise methods. Their reliability is nonetheless not clearly established. These high-resolution methods can be classified in 3 groups: spectral estimation (MUSIC – Multiple Signal Classification – algorithm), parametric subspace-based estimation (ESPRIT – Estimation of Signal Parameter Via Rotational Invariance Techniques – algorithm), and deterministic parameter estimation

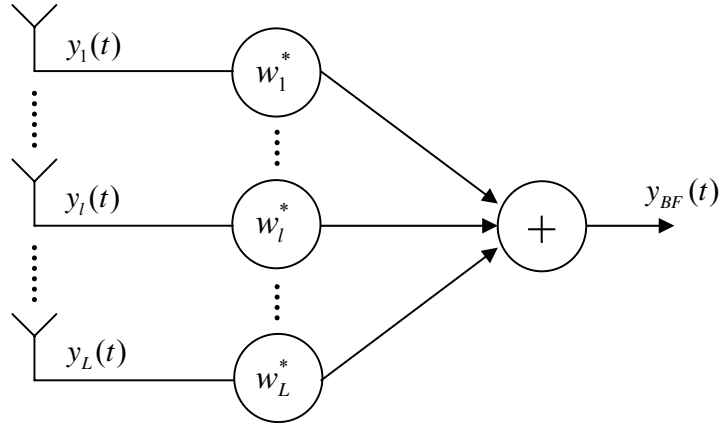


FIG. 3.7: Beamformer structure

(SAGE – Space-Alternating Generalized Expectation-maximization). The present study will concentrate on the first method, for its simplicity and robustness, and on the last method for its suitability for MIMO channel analysis (i.e. beamforming and SAGE).

Beamforming: The principle of beamforming [1] is fairly intuitive: the signals received at the different antennas of the antenna array are multiplied by complex numbered weights w_k (Figure 3.7), aiming the array into a specific direction, that is, “forming a beam”.

Using the notation introduced in the previous chapter, the output of the beamformer can be expressed as (cf. Figure 3.7):

$$y_{BF}(t) = \sum_{l=1}^L w_l^* \cdot y_l(t) = \mathbf{w}^H \cdot \mathbf{y}(t) \quad (3.11)$$

with $\mathbf{w} = [w_1, \dots, w_L]^T$, and where \mathbf{w}^H stands for the Hermitian of \mathbf{w} , i.e. $\mathbf{w}^H = \text{tr}(\mathbf{w}^*)$. Different beamformers exist, depending on the weights chosen. Two different types of weights are presented here.

Conventional Beamformer (or Bartlett Beamformer, or delay-and-sum beamformer):

This method is a natural extension of classical Fourier-based spectral analysis. Weights are chosen to steer the array in the *look* direction (φ_0, θ_0) while maximizing the SNR. If $(\varphi_0, \theta_0) = (\varphi_s, \theta_s)$, then $\mathbf{y}(t)$ can be written as:

$$\mathbf{y}(t) = \mathbf{y}_s(t) + \left(\sum_{i=1, i \neq s}^M \mathbf{y}_i(t) + \mathbf{n}(t) \right) \quad (3.12)$$

As the signal wanted is $\mathbf{y}_s(t)$, the right part of the addition can be considered as a noise $\mathbf{N}_s(t)$. If the following simplified version of equation (2.6) is considered:

$$\mathbf{y}_s(t) = \hat{x}_s(t) \cdot \mathbf{C}(\varphi_s, \theta_s), \quad (3.13)$$

where $\mathbf{C}(\varphi, \theta)$ is the Rx steering vector, i.e. the gain of the Rx antenna array, in the direction (φ, θ) , and $\hat{x}_s(t)$ the signal from s^{th} ray path arriving at the Rx, then maximizing the SNR through matched filtering leads to the following weights:

$$\mathbf{w}_c \propto \mathbf{R}_s^{-1} \cdot \mathbf{C}(\varphi_0, \theta_0), \quad (3.14)$$

with \mathbf{R}_s being the correlation matrix of the noise $\mathbf{N}_s(t)$, defined by:

$$\mathbf{R}_s = E[\mathbf{N}_s(t) \cdot \mathbf{N}_s^H(t)] \quad (3.15)$$

Assuming that the noise is uncorrelated, and that there are no directional interferences, one can choose the following values of the weights:

$$\mathbf{w}_c = \frac{\mathbf{C}_0}{N_0}, \quad (3.16)$$

where $\mathbf{C}_0 = \mathbf{C}(\varphi_0, \theta_0)$, and $N_0 = \mathbf{C}_0^H \cdot \mathbf{C}_0$. This settles a unity response in the look direction. Further details on how to derive these weights can be found in [1]. The output of the beamformer with this \mathbf{w}_c is then:

$$y_{BF}(t) = \hat{x}_s(t) + \mathbf{w}_c^H \cdot \mathbf{n}(t) \quad (3.17)$$

It follows that the mean power P_y of the output can be expressed as:

$$P_y = p_s + p_n, \quad (3.18)$$

where p_s is the power of the ray in the look direction, and p_n the noise power (related to $\mathbf{w}_c^H \cdot \mathbf{n}(t)$). Hence the mean power after conventional beamforming is equal to the power of the source in the direction in which the receiver was directed. The present beamforming method is therefore equivalent to pointing the Rx antenna array to a certain direction mechanically.

Optimal Beamformer (or Capon Beamformer):

The previous method is based on the assumption that no directional interference happens, which is generally not the case in practice: high level sidelobes tend to appear. Nevertheless, the calculation can be resumed from the matched filtering formula (3.14),

given that SNR is maximal. If the beamformer response in the look direction is set to unity, i.e., $\mathbf{w}^H \mathbf{C}_0 = 1$, the following weights are obtained:

$$\mathbf{w}_{opt} = \frac{\mathbf{R}_s^{-1} \mathbf{C}_0}{\mathbf{C}_0^H \mathbf{R}_s^{-1} \mathbf{C}_0} \quad (3.19)$$

In practice the matrix \mathbf{R}_s cannot easily be obtained. As a consequence, it is interesting to express the weights as a function of the correlation matrix \mathbf{R} of the total received signal $\mathbf{y}(t)$. Using (3.12),

$$\mathbf{R} = \mathbf{R}_s + p_s \mathbf{C}_0 \mathbf{C}_0^H, \quad (3.20)$$

The inverse of \mathbf{R}_s can then be derived in terms of \mathbf{R} [1]:

$$\mathbf{R}_s^{-1} = \mathbf{R}^{-1} + \frac{p_s \mathbf{R}^{-1} \mathbf{C}_0 \mathbf{C}_0^H \mathbf{R}^{-1}}{1 - p_s \mathbf{C}_0^H \mathbf{R}^{-1} \mathbf{C}_0} \quad (3.21)$$

yielding to the following expression of the weights:

$$\mathbf{w}_{opt} = \frac{\mathbf{R}^{-1} \mathbf{C}_0}{\mathbf{C}_0^H \mathbf{R}^{-1} \mathbf{C}_0} \quad (3.22)$$

One can prove that the coefficients of optimal beamforming verify:

$$\mathbf{w}_{opt} = \arg \min_{\mathbf{w}} (P_y | \mathbf{w}^H \mathbf{C}_0 = 1), \quad (3.23)$$

that is, the weights correspond to the minimal power maintaining a unity gain in the direction (ϕ_0, θ_0) . This can be understood as a sharp bandpass filter. The method is this way focusing on cancelling the signal in the directions of other sources, at the expense of noise cancelling ability in the look direction.

SAGE (Space-Alternating Generalized Expectation-Maximization): SAGE is a high-resolution algorithm allowing joint estimation of complex weight, relative delay, direction of departure and arrival, as well as Doppler frequency. The algorithm itself has been introduced by Fessler and Hero in 1994 [23], but its application to the MIMO channel data extraction has been extended only later by Fleury in 1999 and 2002 [24]. A quick overview is presented in this subsection.

SAGE is based on an expectation-maximization (EM) method. The SAGE iteration step introduced in the flow graph (Figure 3.8) consists of two steps:

The expectation step: The initial goal of SAGE is to estimate the contribution $\mathbf{y}_i(t)$ of a ray i by maximizing the loglikelihood function associated $\Lambda(\underline{\boldsymbol{\theta}}_i, \mathbf{y}_i)$, where $\underline{\boldsymbol{\theta}}_i$ is the set

of parameters associated with i^{th} ray: its directions of departure and arrival, its propagation delay, Doppler frequency and complex amplitude. The problem is that $\mathbf{y}_i(t)$, and hence $\Lambda(\underline{\boldsymbol{\theta}}_i, \mathbf{y}_i)$, is not observable. Nevertheless, the key idea of EM-like algorithms is to estimate $\Lambda(\underline{\boldsymbol{\theta}}_i, \mathbf{y}_i)$ based on the observation of the total received signal $\mathbf{y}(t)$ and assuming a guess $\hat{\underline{\boldsymbol{\theta}}}$ of $\underline{\boldsymbol{\theta}}$, matrix containing all the $\underline{\boldsymbol{\theta}}_i$. It can then be shown that [24]:

$$E_{\hat{\underline{\boldsymbol{\theta}}}}[\Lambda(\underline{\boldsymbol{\theta}}_i, \mathbf{y}_i(t)) | \mathbf{y}(t)] = \Lambda(\underline{\boldsymbol{\theta}}_i, \hat{\mathbf{y}}_i(t)) \quad (3.24)$$

with $\hat{\mathbf{y}}_i(t) = E_{\hat{\underline{\boldsymbol{\theta}}}}[\mathbf{y}_i(t) | \mathbf{y}(t)] = \mathbf{y}(t) - \sum_{k=1, k \neq i}^M \mathbf{y}(t, \hat{\underline{\boldsymbol{\theta}}}_k)$, where $E_{\hat{\underline{\boldsymbol{\theta}}}}$ is the estimator based on the $\hat{\underline{\boldsymbol{\theta}}}$ estimate of $\underline{\boldsymbol{\theta}}$, and $\mathbf{y}(t, \hat{\underline{\boldsymbol{\theta}}}_k)$ the contribution of a ray with parameters $\hat{\underline{\boldsymbol{\theta}}}_k$.

The maximization step: an estimate of $\underline{\boldsymbol{\theta}}_i$ is then given by:

$$\hat{\underline{\boldsymbol{\theta}}}_i' = \operatorname{argmax}_{\underline{\boldsymbol{\theta}}_i} (\Lambda(\underline{\boldsymbol{\theta}}_i, \hat{\mathbf{y}}_i(t))) \quad (3.25)$$

The maximization of the parameters is done one-by-one: delay, DoA elevation, DoA azimuth, DoD elevation, DoD azimuth, Doppler shift, complex amplitude.

The M iteration steps (for rays $1, \dots, M$) then make one SAGE iteration cycle. During one such cycle, each parameter vector $\underline{\boldsymbol{\theta}}_i$ is estimated once. The cycles (Figure 2.8) stop when a given convergence criterion is achieved.

Note that a maximum number of rays (M) is subsequently introduced.

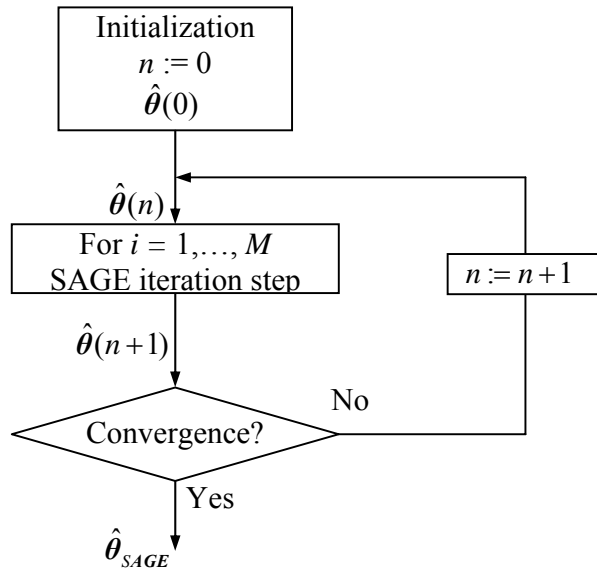


FIG. 3.8: Flow graph of SAGE algorithm

III – 3. Measured parameters and representations

Measured parameters: The final goal of the thesis being capacity coverage prediction, the important parameters are of course pathloss, but also rms (root mean square) delay and angle spreads, which both give information about the correlation of the different paths. Indeed the path correlation influences directly the capacity, hence coverage. For a better understanding of delay spread, study of the PDPs (Power Delay Profiles) is also conducted. The rms delay spread is defined as follows:

$$\tau_{rms\ spread} = \sqrt{\frac{\sum_{i=1}^{N_{paths}} (\tau_i - \bar{\tau})^2 |E_i|^2}{\sum_{i=1}^{N_{paths}} |E_i|^2}}, \quad (3.26)$$

where τ_i is the delay of path i , E_i its complex amplitude, N_{paths} the number of paths and $\bar{\tau}$ the mean delay:

$$\bar{\tau} = \frac{\sum_{i=1}^{N_{paths}} \tau_i |E_i|^2}{\sum_{i=1}^{N_{paths}} |E_i|^2}. \quad (3.27)$$

And similarly, the azimuth (or elevation) angular spread:

$$\phi_{spread} = \sqrt{\frac{\sum_{i=1}^{N_{paths}} \Delta\varphi_i^2 |E_i|^2}{\sum_{i=1}^{N_{paths}} |E_i|^2}}, \quad (3.28)$$

where $\Delta\varphi_i = \varphi_i - \bar{\varphi}$ such as $\Delta\varphi_i \in]-\pi, \pi]$, with φ_i the azimuth (or elevation) angle of path i (departure or arrival) and

$$\bar{\varphi} = \text{atan}_2 \left(\sum_{i=1}^{N_{paths}} E_i^2 \sin \varphi_i, \sum_{i=1}^{N_{paths}} E_i^2 \cos \varphi_i \right) \quad (3.29)$$

where $\text{atan}_2(y, x)$ is the arctangent of y/x , taking into account the sign of both parameters to determine the quadrant of the returned value. This “mean” value $\bar{\varphi}$ does not minimize the angular spread: it corresponds to the angle defined by the center of mass of the angles weighted by the powers of the corresponding paths. Some authors (see e.g. annex A in 3GPP channel model [6]) prefer to define the angular spread as the minimum

over all angles taken as mean value, or to use a 3D angular spread [25]. However, all these angular spread values still indicate a correlation level of the different paths.

Representations: Ray tracing, beamforming and SAGE all provide the multipath components: Direction of Arrival (DoA), Direction of Departure (DoD), delay profile and complex power profile with polarization information. Different representations can be derived from those and are presented in this part. The parameters of interest in the frame of this thesis will then be introduced.

- The angle-delay power profile showed in Figure 3.9 gives the azimuth angles of arrival (angular axe) and the delay (radial axe) of the different paths, summed over all snapshots, and power information is given by the colorbar. The delays are normalized: the 0 ns reference corresponds to the shortest path. This graph allows identifying the different groups of rays. On the graph presented, we can e.g. see 3 “waves” of rays arriving from the top (angle of 90°).
- The delay/snapshot power profile in Figure 3.10 gives the delay of the paths as a function of the traveled distance of the receiver, and colors again indicate the power. It corresponds to the variations of a Power Delay Profile (PDP), thus allowing observing the behavior of the shortest path and the dependence of the PDP on the environment. For instance in Figure 3.10, the receiver is turning at 47 m to a parallel street (from a perpendicular street), thus reducing the spectrum power and the spread of delays.

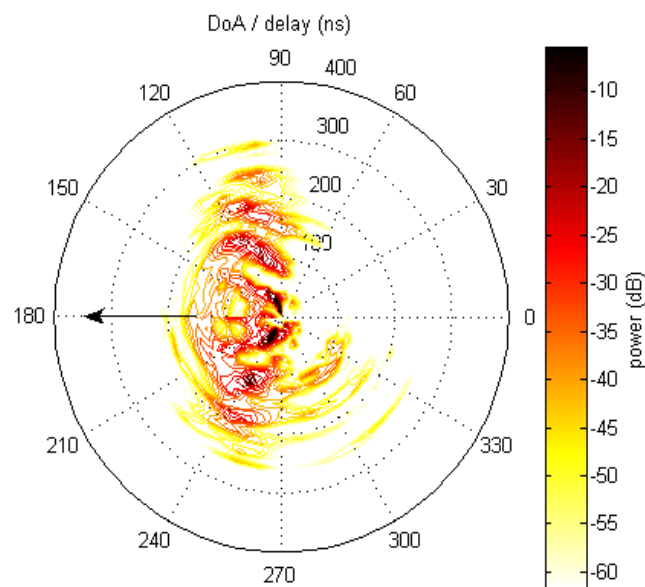


FIG. 3.9: Delay angular profile

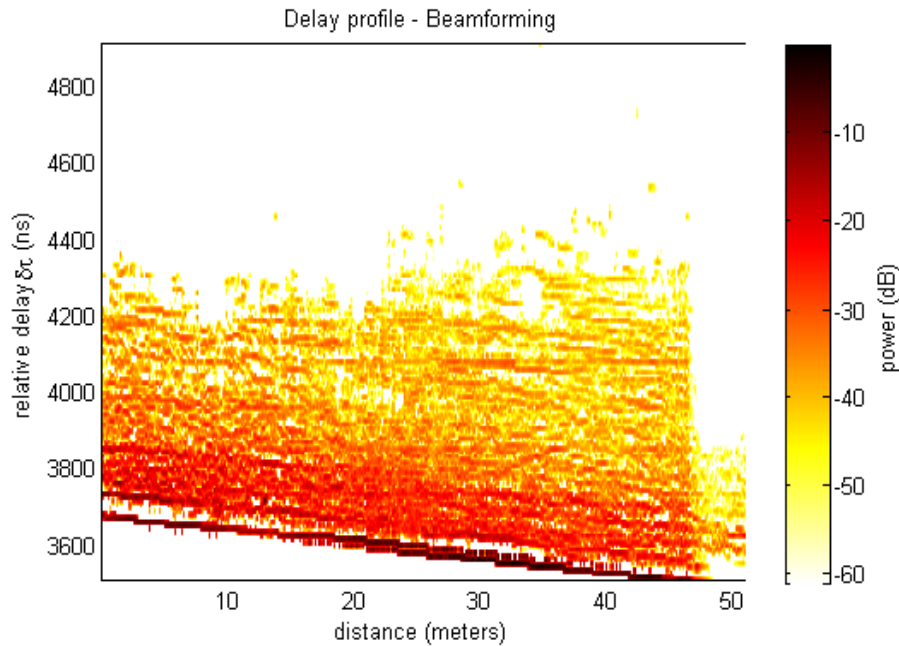


FIG. 3.10: Delay/snapshot profile

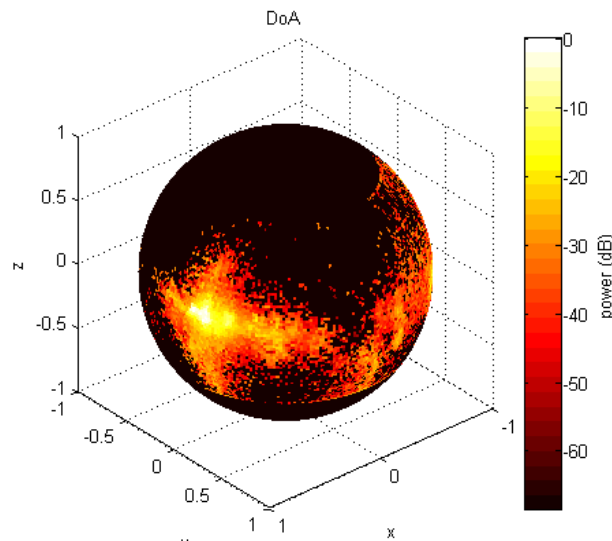


FIG. 3.11: 3D direction of arrival profile

- The 3D graph of Figure 3.11 shows the Direction of Arrival (DoA) of all the rays over a specified distance. Power information is displayed through the color gradation. This 3D graph allows a better view of angular information than the two traditional 2D graphs (azimuth angle of arrival and elevation angle of arrival), which disregard the horizontal/vertical correlation. From Figure 2.11 it can be inferred that the spread of elevation angle corresponds to a given azimuth angle, and vice-versa.

- Through Figure 3.12, one can see the impact of the environment; the channel characteristics are displayed on the geographical map by color gradation. Here the information considered is the rms delay spread calculated from ray tracing; the LOS/NLOS distinction can be clearly seen (base station location on the right, indicated by BS).

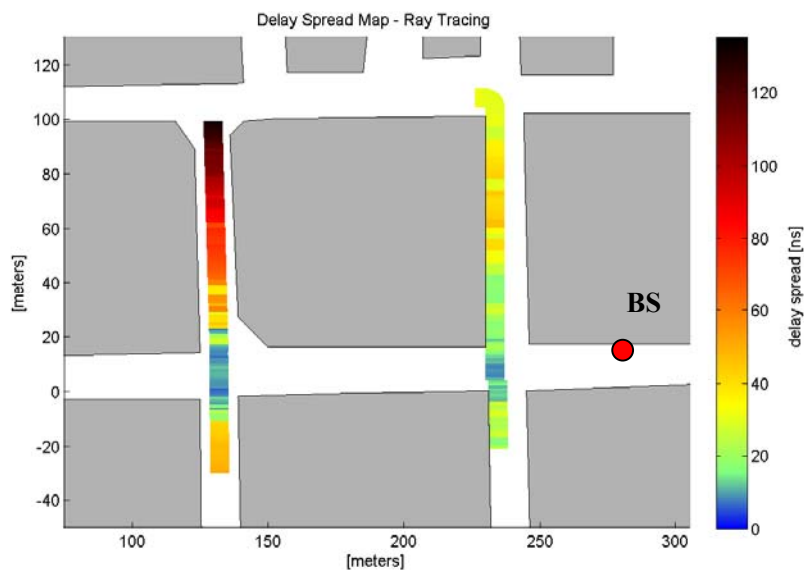
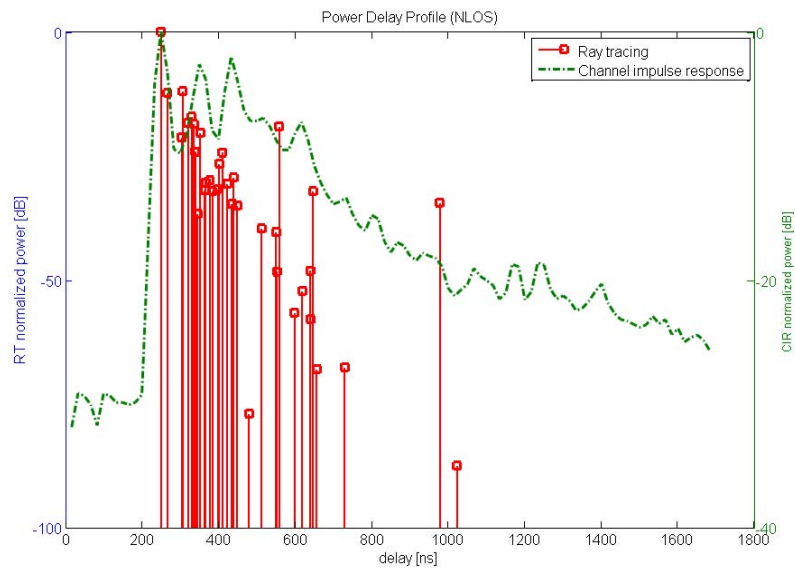
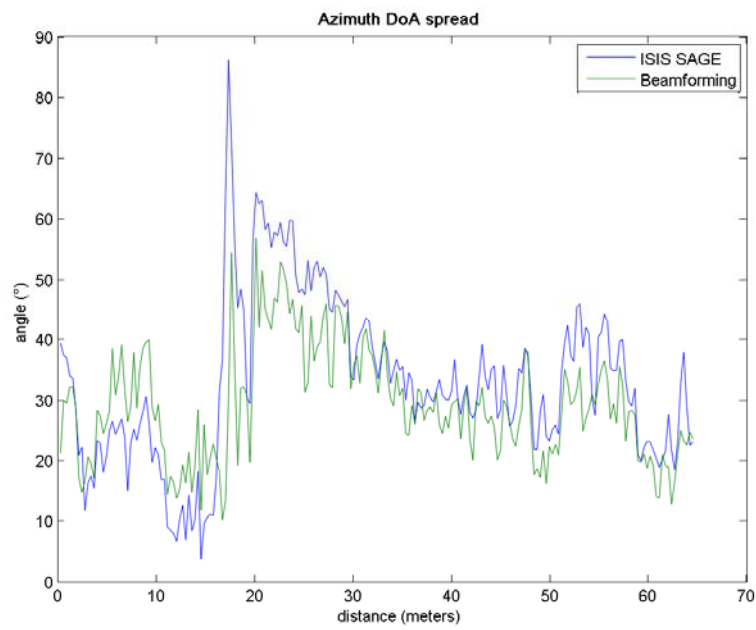


FIG. 3.12: *Delay spread map*

- More traditional graphs are also of great interest, such as e.g. the power delay profile (see Figure 3.13), or the azimuth angular spread (Figure 3.14). The PDP displayed here shows the continuous PDP derived from Channel Impulse Responses (CIR), and the discrete one given by ray tracing, whereas the presented azimuth angular spreads are derived from SAGE (blue curve) and beamforming (green curve).

Comparison is difficult if the representation is different from the usual 2D graphs, nonetheless the other types of graphs are still interesting for understanding the channel and when investigating it on a precise matter.

**FIG. 3.13:** *Power delay profile***FIG. 3.14:** *Azimuth angular spread*

IV – Measurements and results

In this part the measurement equipment and campaign are first presented. Then, now that the two types of relevant methods have been introduced, together with the key channel parameters, a comparison between the deterministic method ray tracing and the data extracted from measurements is conducted, based on delay and angular spreads.

IV – 1. Environment, sounder characteristics and parameters of algorithms

Channel measurements were performed on April 19, 2004 during the evening (21:00-23:30) in the center of Helsinki for a center frequency of 5.3 GHz, by means of a wideband MIMO radio channel sounder developed at Helsinki University of Technology [21, 22]. The channel measurement is done first by a matched filtering sliding correlator, later by direct digital sampling, where the impulse response is detected by digital post processing [21]. In the transmitter, the 5.3 GHz carrier is modulated by a maximum length pseudo-noise code at a chip rate of 60 MHz.

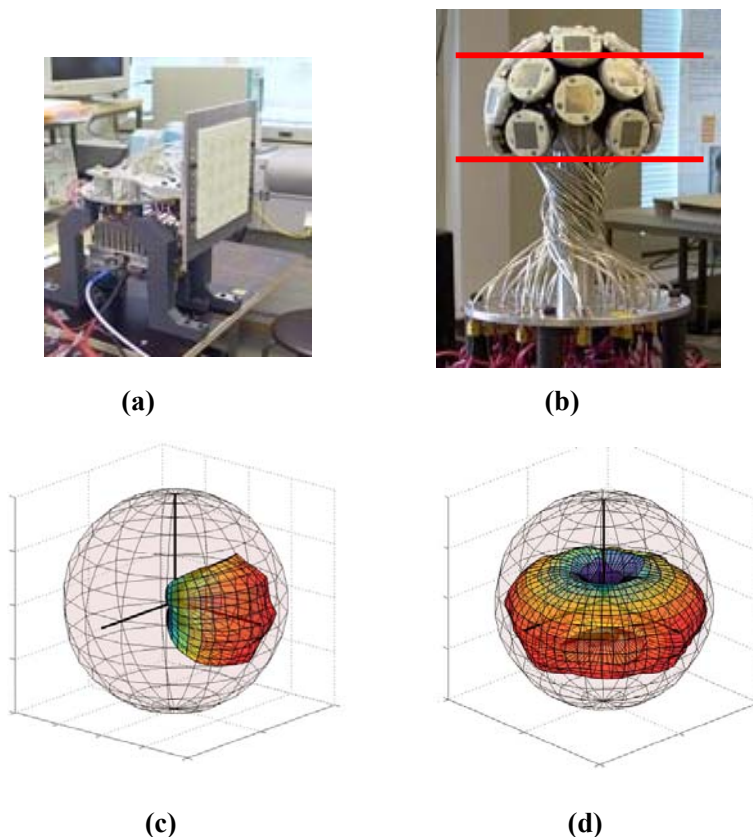


FIG. 4.1: Antenna arrays and corresponding measured amplitude responses

The MIMO matrix of the measurement was limited to a 32×32 size. This limitation was chosen for the following reasons: hardware complexity, amount of measurement data and measurement coherence time.

The transmitting antenna was a 4×4 slanted dual-polarized planar array (Figure 4.1a). The 3D antenna gain is displayed in Figure 4.1c, highlighting the directivity of the antenna. This planar array was located on a crane at 10 m height. The transmitter is therefore below the rooftops of surrounding buildings, as those are at a height of 25 m on average: it corresponds to a microcell configuration. One channel is disconnected to connect a load on the switch, and another to a discone antenna, both to provide calibration data for offline processing. The transmitting power was 36 dBm.

The receiving antenna was a semi-spherical antenna array with 21 dual-polarized elements (Figure 4.1b); only the 15 lowest elements were used (elements between the two red lines on the Figure 4.1b). The MIMO system considered is thus 30×30 . The 3D antenna gain is displayed in Figure 4.1d; the antenna array behaves like an omnidirectional antenna in the horizontal plane, but in the vertical plane its visibility is limited outside the elevation interval $[-40^\circ; 40^\circ]$. The receiver was moved along microcellular routes (Figure 4.2) on a trolley, at a height of 1.6 m, measuring the channel approximately every fourth of wavelength (thus every 1.4 cm).

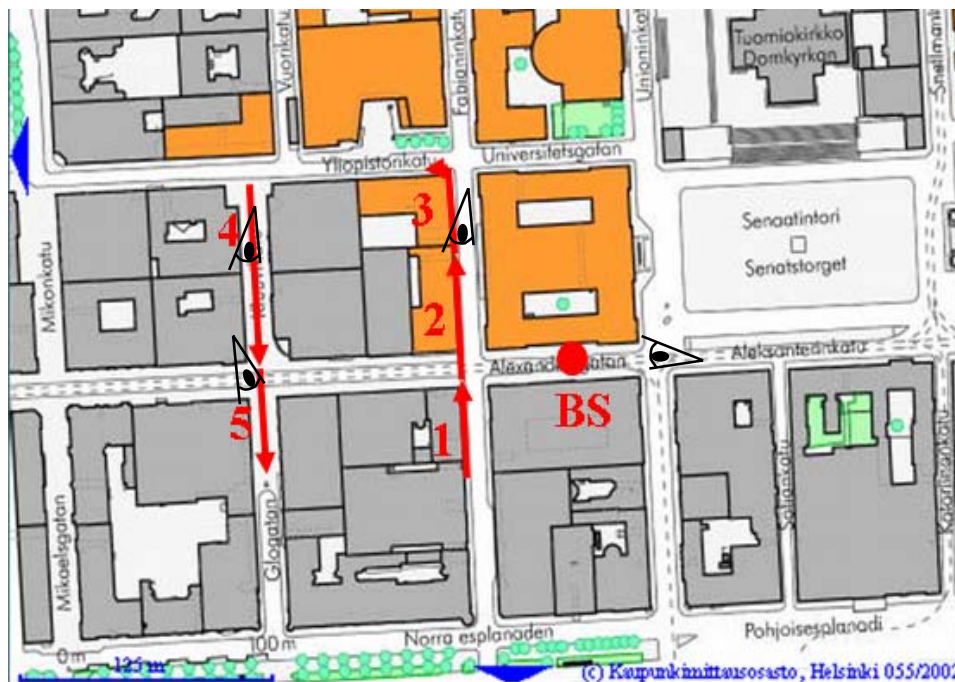


FIG. 4.2: Measurement routes considered (1 to 5)

In this study, we will only consider the first 5 routes, which correspond to two transversal streets in the vicinity of the transmitter (Figures 4.2 and 4.3). The total distance traveled is then about 250 m, and the Tx-Rx distance varies between 75 and 170 m. In the following, routes 1, 2 and 3 are logically referred as 1st street, and routes 4 and 5 as 2nd street. The Figure 4.4 represents the map data used in ray tracing, which also takes into

account the Digital Terrain Model (DTM), i.e. the ground heights (Figure 4.5). The precision of the map is 1 cm (accuracy of about 1 m) in horizontal plane (Figure 4.4) and 1 m in the vertical plane (Figure 4.5). The map just contains the different buildings with their heights, no details, such as balconies, wall irregularities, street furniture (lamp posts, bus stops, street signs, benches, ...), are provided. The inaccuracy of the map and its limited content will naturally influence ray tracing results.

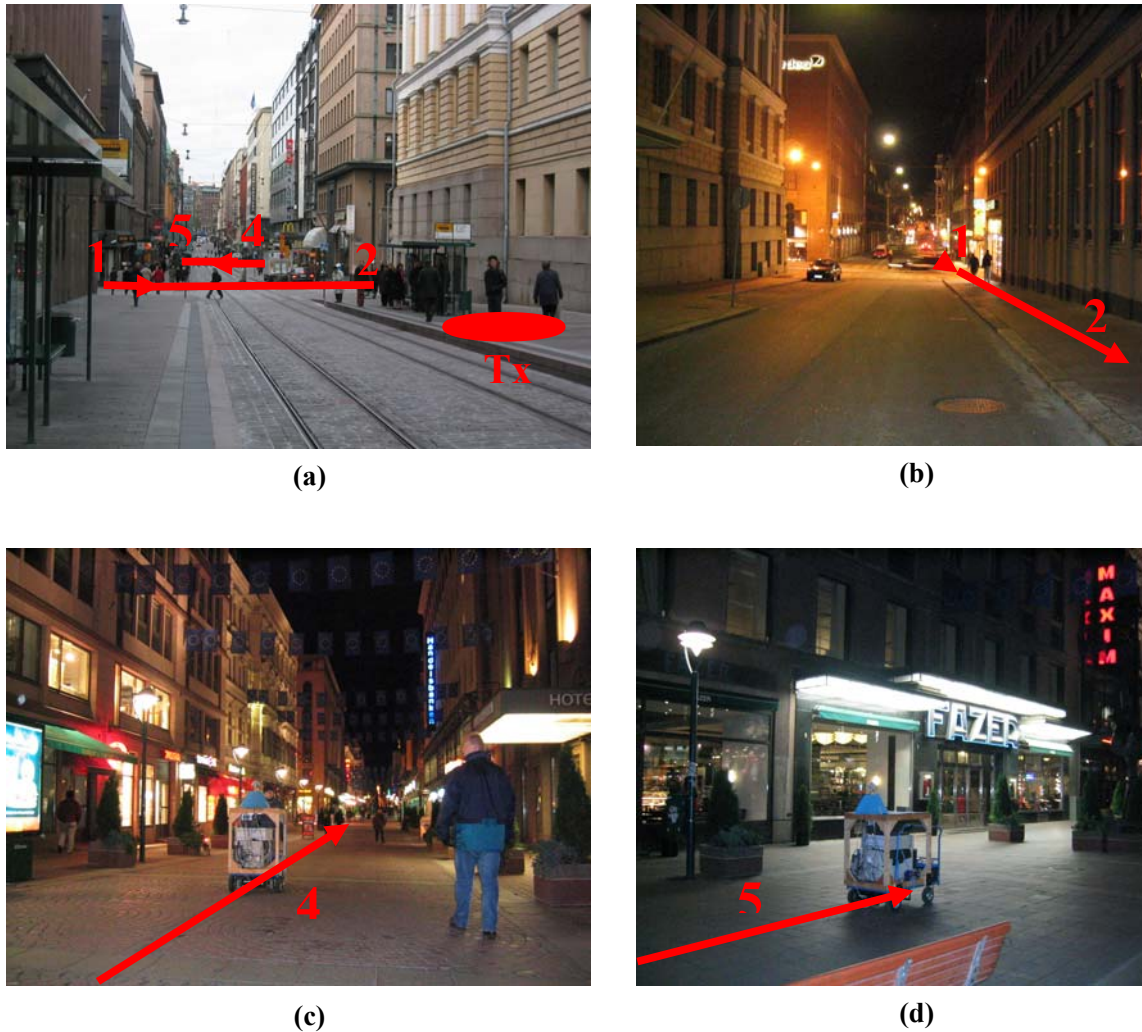


FIG. 4.3: Views of the measurement routes
(see eye markers on Figure 4.2)

The SAGE results have been provided by Elektrobit's ISIS software. The maximum number of paths for the SAGE algorithm has been set to 30, and for the beamforming method to 100 (a limit of 50 paths per polarization at the receiver; this limit hasn't been reached on the routes considered). The SAGE limit is nevertheless quite restrictive, especially in LOS (Line Of Sight) case. Actually, the algorithm is then "blinded" by the strong direct path: it often finds 30 paths really close (in delay scale) to the direct path.

Note that SAGE computation time is already about one week per route (there are approximately 3000 snapshots per route), and the calculation time grows exponentially, hence this limit is still judicious in the frame of this thesis.



FIG. 4.4: Map data

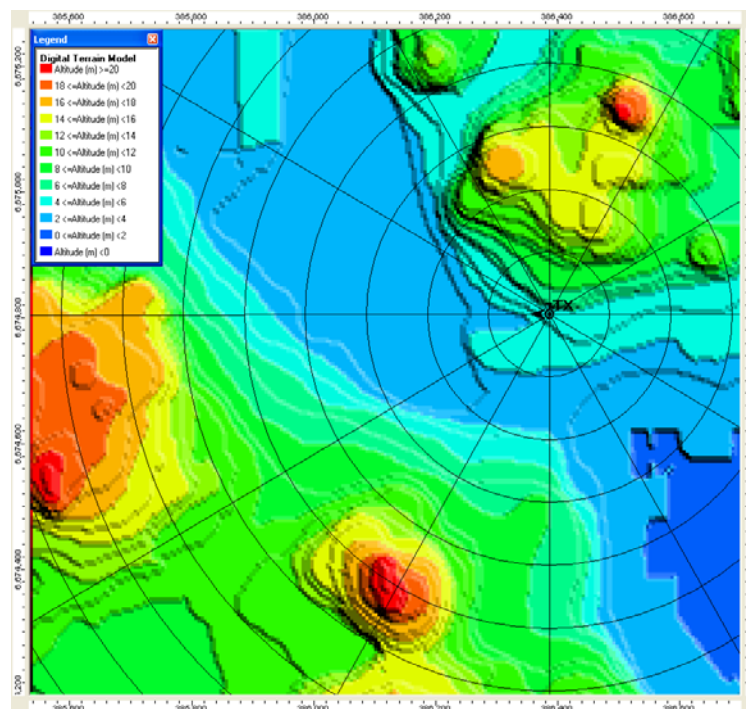


FIG. 4.5: Heights on the studied zone

The restriction on ray tracing is 1 diffraction, 5 reflections, and no reflections occurring after diffraction (note that a diffraction point behaves actually as a secondary source). These parameters have been set as the best quality/computation time tradeoff. It has moreover been observed that a ray which undergoes more than 1 diffraction, or more than 5 reflections, doesn't have a significant contribution to the different channel characteristics considered. For the two measurement streets, the calculation took tens of seconds (1 meter resolution, thus about 250 points), but if the calculation is extended to the whole zone displayed in Figures 4.3 and 4.4, the computation time was about 30 minutes (5 meter resolution, thus around 30,000 points).

IV – 2. Comparisons between SAGE and Ray Tracing

As discussed previously in III.3, the first comparisons will be based on pathloss, PDP, delay spread and azimuth angular spread. Beamforming would only be used when path information can be seen (i.e. only for PDPs). Indeed SAGE omits the paths far in delay from the strongest path, due to the 30 paths limitation. As mentioned previously, this limitation might influence the results especially in LOS cases. But, even if beamforming finds rays further delay-wise, its angular resolution (about 30°) makes the path separation difficult next to the strongest path, thus biasing the delay and angular spread values (in case of several paths in a close delay range).

Pathloss: Ray tracing has already been proven effective for pathloss prediction in many publications, and also, in particular, for the software used in this work. However, a quick comparison along the 2 streets is still made between ray tracing and SAGE (Figure 4.6, together with Tx-Rx distance). The mean difference is then 0.02 dB, and the standard deviation is 4.45 dB. Note that SAGE results have been normalized to minimize the mean error, as no absolute power is provided. The values displayed in Figure 4.6 are derived considering antenna gain and transmitted power.

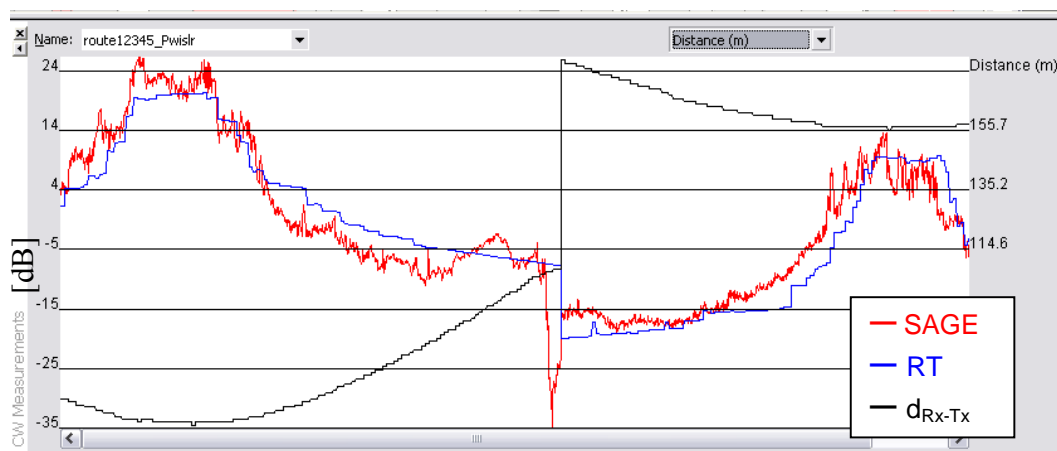


FIG. 4.6: Pathloss derived from SAGE and RT

Power delay profiles: In order to have a reliable reference, the power delay profile is also derived from the channel impulse responses (CIRs). The comparison of PDPs derived from CIR, ray tracing, SAGE and beamforming has been conducted for several dozens of snapshots, among which two representative snapshots are here presented in Figures 4.7 (NLOS case) and 4.8 (LOS case). Powers have been normalized for each snapshot, and time scales have been translated so that the different quickest rays coincide. The PDPs derived from the different methods seem coherent (Figures 4.7 and 4.8). The slopes are the same for SAGE, beamforming and CIR in NLOS and LOS, but ray tracing

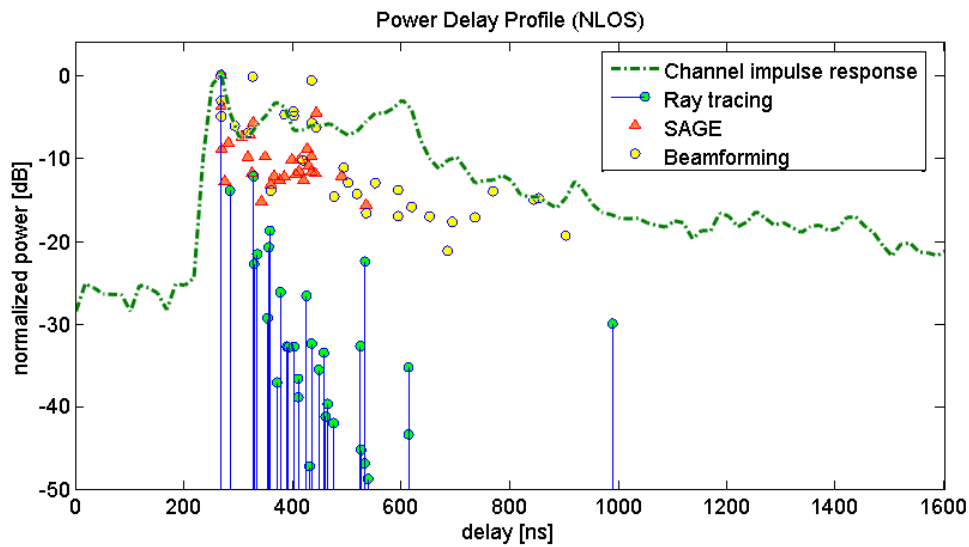


FIG. 4.7: NLOS Power Delay Profiles from RT, SAGE, Beamforming and CIR (beginning of route 3)

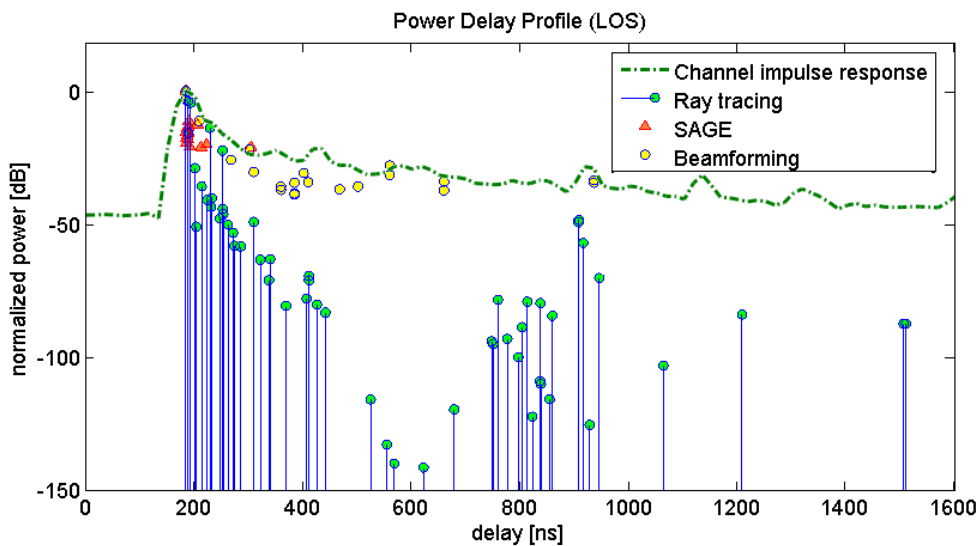


FIG. 4.8: LOS Power Delay Profiles from RT, SAGE, Beamforming and CIR (beginning of route 2)

results produce a higher slope, overestimating the power of the first rays. Nonetheless, this is compensated by the fact that these first rays are scarce compared to those derived from SAGE: e.g., in Figure 4.7, ray tracing only finds 2 rays next to the quickest path, instead of 5 rays for SAGE, but for ray tracing the quickest ray is 15 dB stronger than all other rays, instead of 5 dB for SAGE. These 5 different rays derived from SAGE have moreover close spatial components (DoA and DoD), and thus might correspond to a single path. Besides, the results of the comparisons made in the next pages support this compensation hypothesis.

The limitation of number of paths in SAGE can also clearly be seen, especially in the LOS case, where the method is “blinded” by the strongest ray. In addition beamforming and ray tracing derive rays quite far from the strongest ray (delay-wise): SAGE does not find rays with a delay above 500 ns, while for beamforming the limit is around 1000 ns, and for ray tracing’s 1500 ns. On a (normalized) power scale, the resolution range is about 20 dB for SAGE, 25 dB for beamforming and more than 50 dB for ray tracing.

(RMS) Delay spreads: Next to Line of Sight, the two derived delay spreads (Figure 4.9) closely follow the same variations: low values in LOS, increasing when getting away from LOS. But RT does not coincide well with SAGE further than 20 meters from LOS position, especially 80 meters from LOS: on both streets the delay spread derived from ray tracing is then decreasing too abruptly compared to SAGE delay spread. In both cases it corresponds to one of the strongest path which is at this distance obstructed by a building; in ray tracing the path does not go through, whereas in reality, according to SAGE, the power of this path is attenuated but it is still reaching the receiver (thanks to the beamwidth of the ray, or a curved path).

In addition, note that, based on SAGE results, the variations at LOS/NLOS limit are not really steep, contrary to azimuth angular spread. As an important difference of path correlation level between LOS and NLOS was expected, delay spread might not be a good path correlation indicator for these zones.

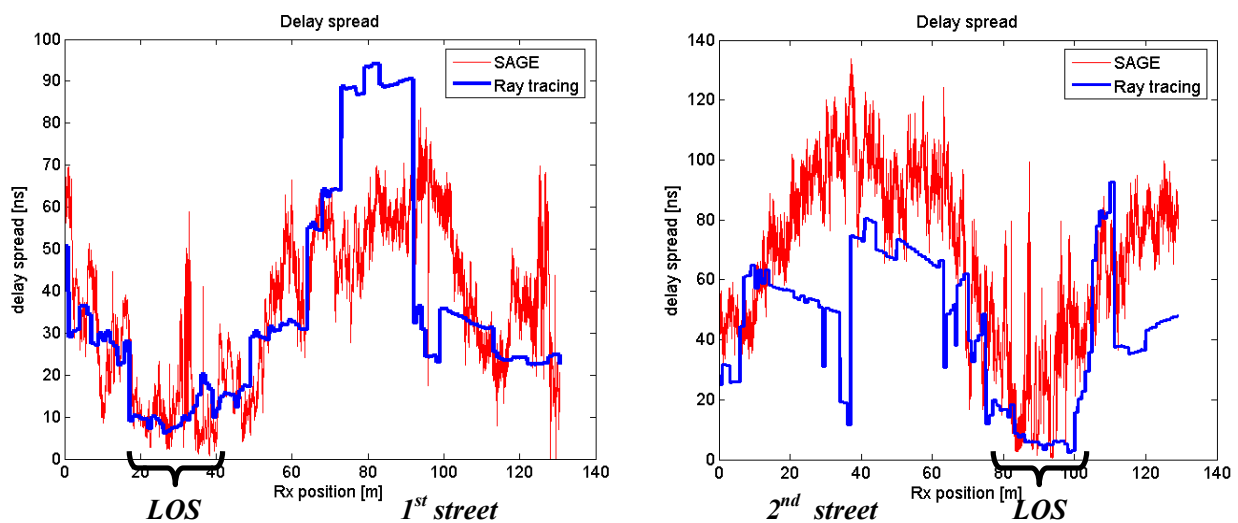


FIG. 4.9: Delay spreads derived from SAGE and RT

Azimuth angular spreads: RT azimuth angle spread follows the same variation as SAGE, in LOS and NLOS conditions (Figure 4.10). No major difference between the two methods can be noted, and the visible differences between the curves in Figure 4.10 are statistically reasonably small (Table 4.1). Some peaks in LOS can be noticed which were also present in delay spread comparison. One possible reason can be seen in Figure 4.3a: one can notice the tramway stop which is between transmitter and receiver on the zone of interest. It is probably provoking a higher spread in angle and delay domains by diffracting or reflecting the rays. It is also interesting to note the high values in the vicinity of LOS, due to diffraction by the building edges, with a jump from a low spread (around 10°) in LOS to a high spread (around 70°) in NLOS, in less than 10 m. Capacity will undergo a similar steep increase in these zones, as moreover the SNR is there still high.

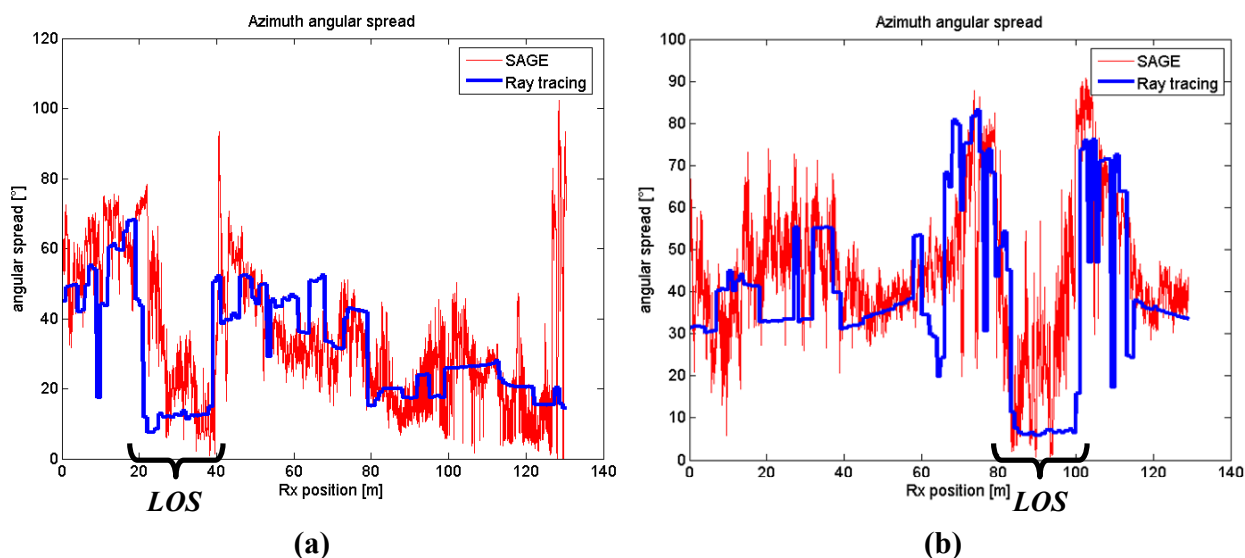


FIG. 4.10: Azimuth angular spreads derived from SAGE and RT
(a) 1st street, (b) 2nd street

TABLE 4.1: Azimuth angular spreads derived from SAGE and RT: statistics

	mean difference	standard deviation
1 st street	1.9°	18.5°
2 nd street	5.5°	18.2°

V – Application: capacity coverage

Ray tracing prediction of delay spread and azimuth angular spread agree with SAGE results on a global scale. Capacity coverage does not usually provide a 1x1 m² or finer resolution map, but rather a 5x5 - 10x10 m². Hence, the comparison can proceed: capacity itself will now be computed and ray tracing and SAGE compared based on this parameter, with the final goal of providing capacity coverage.

V-1 MIMO capacity

The channel capacity of a memoryless wireless channel, with random variable X as input and random variable Y as output, is defined as [26]

$$C = \max_{p(x)} \mathcal{I}(X;Y) \quad (5.1)$$

where the maximization is done over all $p(x)$ possible statistical distributions for the transmitter. $\mathcal{I}(X;Y)$ is the mutual information between random variables X and Y , which can be written as

$$\mathcal{I}(X;Y) = \mathcal{H}(Y) - \mathcal{H}(Y|X), \quad (5.2)$$

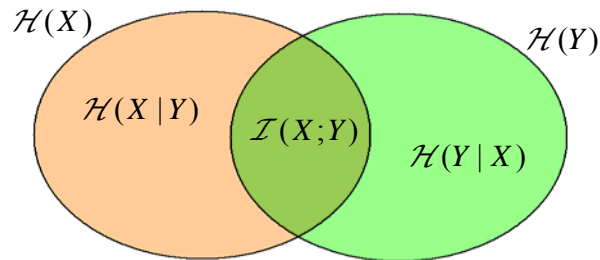


FIG. 5.1: Entropy and mutual information

with $\mathcal{H}(Y)$ being the entropy of random variable Y , and $\mathcal{H}(Y|X)$ the conditional entropy of Y given X . The equality states that the mutual information of X and Y is the entropy (i.e. uncertainty, i.e. information) at the receiver, of which should be subtracted the entropy of Y given that the value of X is known (Figure 5.1).

A $N_R \times N_T$ MIMO system is usually represented by the following notation (narrowband AWGN -Additive White Gaussian Noise- channel model):

$$\mathbf{y} = \mathbf{H}\mathbf{x} + \mathbf{n}. \quad (5.3)$$

The *ergodic channel capacity* of the random MIMO channel considered represents the average value of the capacity over the distribution of the channel matrix \mathbf{H} . It can then be expressed as [27]

$$\mathcal{C} = E_H \left\{ \max_{p(\mathbf{x})|P_{Tx} \leq P_0} \mathcal{I}(\mathbf{x}; \mathbf{y}) \right\}, \quad (5.4)$$

where E_H is the expectation over the channel realizations, and $P_{Tx} \leq P_0$ the constraint in the total transmitting power, which can also be written as

$$\text{tr}(\boldsymbol{\phi}) \leq P_0, \quad (5.5)$$

with P_0 the maximum total transmitting power, and $\boldsymbol{\phi} = E\{\mathbf{x}\mathbf{x}^H\}$ being the covariance matrix of the transmitted signal \mathbf{x} , knowing that

$$P_{Tx} = E\{\mathbf{x}^H\mathbf{x}\} = E\{\text{tr}(\mathbf{x}^H\mathbf{x})\} = E\{\text{tr}(\mathbf{x}\mathbf{x}^H)\} = \text{tr}(\boldsymbol{\phi}). \quad (5.6)$$

Another measure often used for expressing channel capacity is the *outage channel capacity*. It quantifies a level of performance guaranteed with a certain level of confidence: the $q\%$ outage capacity represents the capacity guaranteed for $(100 - q)\%$ of the channel realization [27].

$$\mathcal{P} \left\{ \max_{p(\mathbf{x})|P_{Tx} \leq P_0} \mathcal{I}(\mathbf{x}; \mathbf{y}) < \mathcal{C}_{q\% \text{ outage}} \right\} = q\%. \quad (5.7)$$

By using (5.2) and (5.3), the mutual information can be written as

$$\begin{aligned} \mathcal{I}(\mathbf{x}; \mathbf{y}) &= \mathcal{H}(\mathbf{y}) - \mathcal{H}(\mathbf{y} = \mathbf{H}\mathbf{x} + \mathbf{n} | \mathbf{x}) \\ &= \mathcal{H}(\mathbf{y}) - \mathcal{H}(\mathbf{n}), \end{aligned} \quad (5.8)$$

making the reasonable assumption that the transmitted signal \underline{x} and the noise \underline{n} are independent. As $\mathcal{H}(\mathbf{n})$ is fixed, we only need to maximize $\mathcal{H}(\mathbf{y})$. The entropy $\mathcal{H}(\mathbf{z})$ of a complex random variable is maximized when \mathbf{z} is a circularly symmetric complex Gaussian [28], and

$$\mathcal{H}(\underline{z}) = \log |\pi e \mathbf{Q}|, \quad (5.9)$$

where \mathbf{Q} denotes the covariance matrix of \mathbf{z} , and $|\cdot|$ the determinant operation. If \mathbf{x} is a circularly symmetric complex Gaussian, then so is $\mathbf{H}\mathbf{x}$ [28]. Assuming the noise is also circularly symmetric, equation (5.8) can then be simplified as follows [27, 28]:

$$\mathcal{L}(\mathbf{x}; \mathbf{y}) = \log_2 \left| \mathbf{I}_{N_R} + \mathbf{H}\phi\mathbf{H}^H (\mathbf{R}_n)^{-1} \right|, \quad (5.10)$$

where \mathbf{R}_n is the covariance matrix of the noise. Without knowledge of the channel, choosing $\phi = \frac{P_0}{N_T} \mathbf{I}_{N_T}$ (i.e. uniform power distribution at the transmitter and independent x_i) is maximizing the mutual information. Assuming that the different components of the noise vector are uncorrelated, $\mathbf{R}_n = \sigma_n^2 \mathbf{I}_{N_T}$ and the ergodic capacity of the AWGN MIMO channel can eventually be expressed as [27]

$$\mathcal{C} = E_H \left\{ \log_2 \left| \mathbf{I}_{N_R} + \frac{P_0}{\sigma_n^2 N_T} \mathbf{H}\mathbf{H}^H \right| \right\}, \quad (5.11)$$

σ_n^2 being the noise power. If considering the normalized channel matrix $\tilde{\mathbf{H}}$, obtained as follows:

$$\tilde{\mathbf{H}} = \frac{\mathbf{H}}{\alpha_{Fr}}, \quad (5.12)$$

where $\alpha_{Fr} = \frac{\|\mathbf{H}\|_F}{\sqrt{N_R N_T}}$, the *average SNR at each receiver branch* ρ can be defined in terms of the total transmitted power P_0 and of the noise power σ_n^2 [29]

$$\rho = \frac{P_0}{\sigma_n^2}. \quad (5.13)$$

This can be intuited by looking into the relations linking ρ and P_0 :

$$\rho = \frac{P_{Rx}/N_R}{\sigma_n^2} = \frac{\sum_{i=1}^{N_R} |y_i|^2}{N_R \sigma_n^2} \leq \frac{\sum_{i=1}^{N_R} \sum_{k=1}^{N_T} |H_{ik} x_k|^2}{N_R \sigma_n^2} = \frac{P_0 \|\mathbf{H}\|_F^2}{N_R N_T \sigma_n^2} = \frac{P_0}{\sigma_n^2} \alpha_{Fr}^2 \quad (5.14)$$

Hence equation (5.11) can then be expressed in terms of ρ and $\tilde{\mathbf{H}}$ [30]: (Foschini-Telatar formula)

$$\mathcal{C} = E_H \left\{ \log_2 \left| \mathbf{I}_{N_R} + \frac{\rho}{N_T} \tilde{\mathbf{H}} \tilde{\mathbf{H}}^H \right| \right\} \quad (5.15)$$

Using the eigenvalue decomposition of $\mathbf{H}\mathbf{H}^H$ in (5.11) (as $\mathbf{H}\mathbf{H}^H$ is hermitian), or the singular value decomposition of \mathbf{H} , one can also obtain an alternative expression of the capacity [27]:

$$\mathcal{C} = E_H \left\{ \sum_{i=1}^{\text{rank}(\mathbf{H})} \log_2 \left(1 + \frac{P_0}{\sigma_n^2 N_T} \lambda_i \right) \right\} \quad (5.16)$$

or again:

$$\mathcal{C} = E_H \left\{ \sum_{i=1}^{\text{rank}(\mathbf{H})} \log_2 \left(1 + \frac{P_0}{\sigma_n^2 N_T} \mu_i^2 \right) \right\} \quad (5.17)$$

where the λ_i are the eigenvalues of $\mathbf{H}\mathbf{H}^H$ and μ_i the singular values of \mathbf{H} ; this underlines better the parallel subchannels underlying in the MIMO system than equations (5.11) or (5.15). It also brings to light the linear grow with N of the $N \times N$ MIMO capacity.

V-2 Coverage planning

Channel reconstruction: The measurement campaign considered in this thesis is using a 30x30 MIMO system. To derive coverage, amore realistic system (and antennas) should be used. To that end, a channel reconstruction tool called MEBAT is used [31, 32]. The channel responses are derived from the antenna radiation patterns at the transmitter and the receiver, and from the channel parameters (directions of departure and arrival, received signal for different polarizations) derived by SAGE or ray tracing (Figure 5.2). The delays are not taken into account, as a narrowband assumption is made to decrease the computational burden.

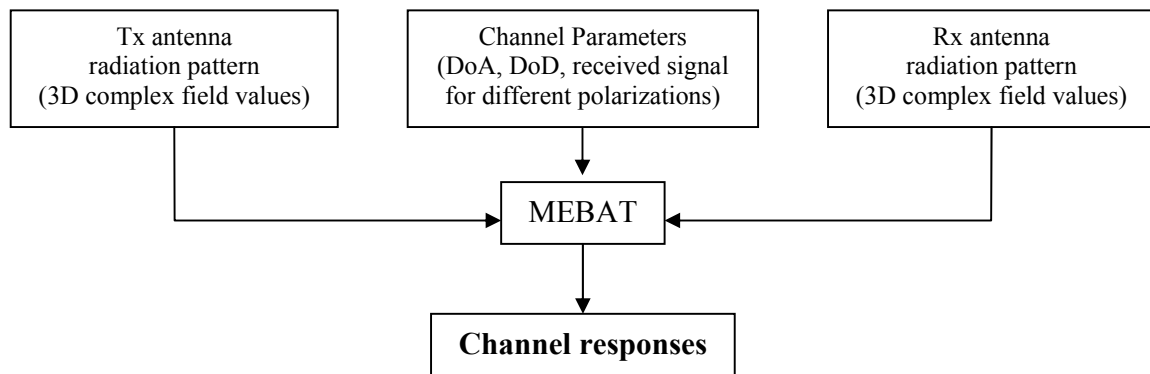


FIG. 5.2: MEBAT principle

The dimension of the MIMO system chosen is 4x4. The antenna arrays used are both dual-polarized. Considered polarizations are vertical and horizontal polarizations. The transmitting antenna is west-oriented like in the measurements, and consists of two half-wavelength dual-polarized square patches pointing the same direction (Figure 5.3). The receiving antenna is an array of half-wavelength dipoles (Figure 5.4).

Random phases method: Ray tracing and high-resolution algorithms results provide just one realization of the channel, as only one single measurement has been done for a given position. The computation of the capacity CDF (Cumulate Distribution Function) would in fact require a large number of measurements for each point, slightly moving the scatterers and the antenna arrays between two successive measurements. This huge effort can be avoided by emulating the channel randomness; the phases of the multipath complex amplitudes are randomly changed [33]. These phases are actually often considered as uniformly distributed random variable [34], whose different realizations represents the movements of the receiver (or the transmitter) and of the scatterers. Moreover this method also eludes the problem of calculating phases for ray tracing, as the various approximations (propagation model, map data, ...) hinder a reliable estimation of the phases.

As in [33], a quick study has been made to justify the use of random phases. The channel realization considered was obtained from the measurements through SAGE algorithm, and average SNR at each receiver branch was supposed to be 10 dB. The CDF of the capacity was calculated with 3 different methods:

- (i) at a given snapshot with the random phases method (10,000 occurrences)
- (ii) with 9 samples of the channel matrix, obtained by moving the receiver forward/backward by steps of $\lambda/4$ (corresponding to the distance between two consecutive snapshots in measurements)
- (iii) simulating the previous mentioned movement, through calculation of the phase shifts of the multipath components induced by this translation:

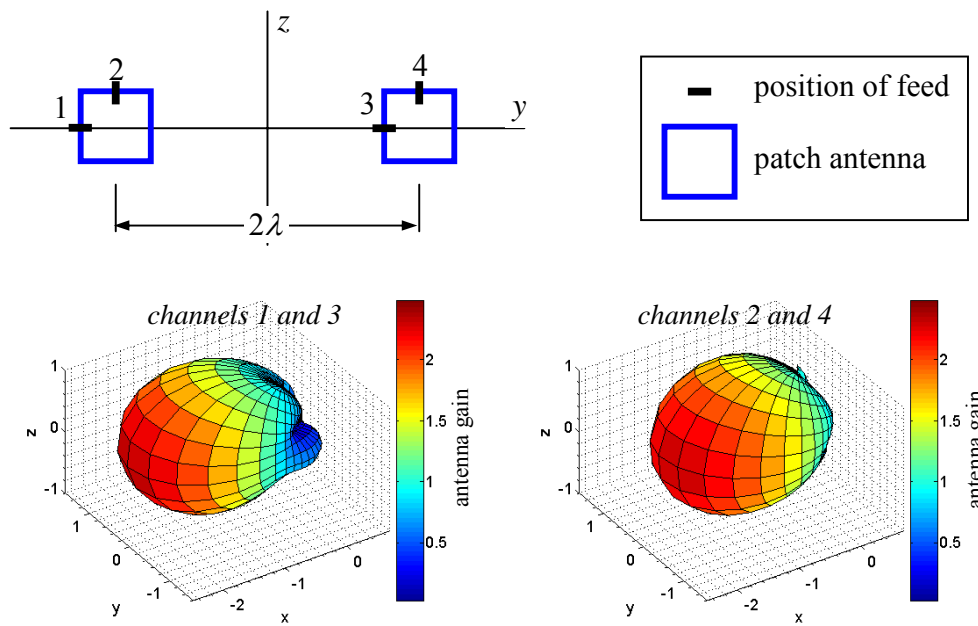


FIG. 5.3: Tx antenna array: geometry and amplitude response

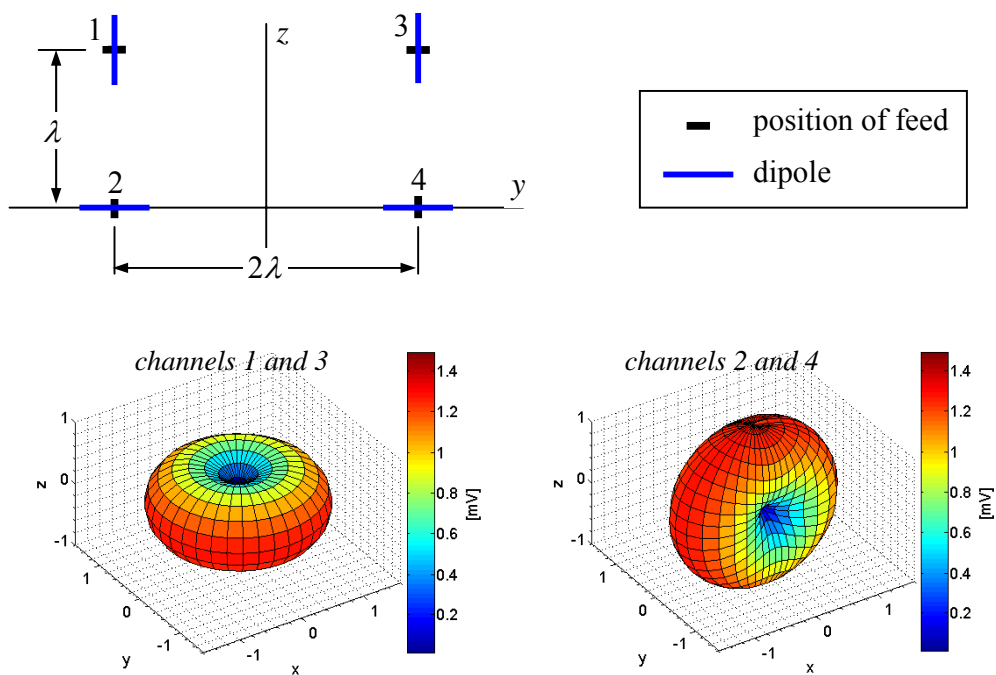


FIG. 5.4: Rx antenna array: geometry and amplitude response

$$\Delta\delta_k = \lambda \cdot \Delta\varphi_k = \frac{k\lambda}{4} \cos(\phi), \quad (5.18)$$

with $k \in \llbracket -4 ; 4 \rrbracket$, where λ is the wavelength, $\Delta\delta_k$ is the OPD (optical path difference) between the reference position and a k -snapshots translated position, considering a ray with azimuth direction of arrival ϕ , and $\Delta\varphi_k$ is the respective phase shift (Figure 5.5).

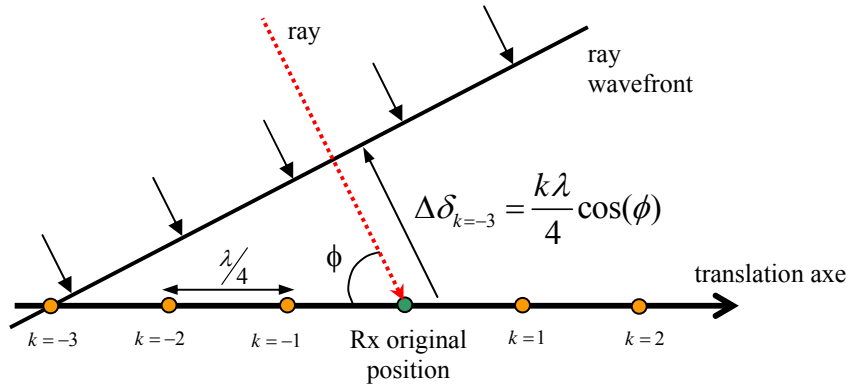


FIG. 5.5: Emulated translation method: phase calculation

Several (about 20) snapshots were considered. The representative results obtained for one of them can be seen in Figure 5.6: the 3 aforementioned methods are displayed together with the capacity calculated directly from single channel realization of the measurements. The 3 methods always give close results. In this case the measured value (“initial capacity” in Figure 5.6) corresponds to the mean capacity of the CDFs of methods (i) and (iii). Compared to these two methods, the method (ii) provides a CDF translated of 1bps/Hz toward smaller values. One possible reason is that the $\lambda/4$ step is too big for the considered environment. Nonetheless it is worth mentioning that the random phases method might sometimes enhance the capacity by artificially decorrelating the different MIMO paths, as the random phases added are independent between the different paths. On some snapshots considered the initial capacity actually corresponds to a 20% outage capacity, even if on some others (nonetheless rarer) it corresponds to an 80% outage capacity.

Note that the computation time varies between the methods: the random phase method took about 60 minutes (MEBAT tool was optimized to get this computation time), whereas the 2 others took less than 1 minute. If considered reliable enough, it could thus be interesting to use them to estimate the capacity CDF.

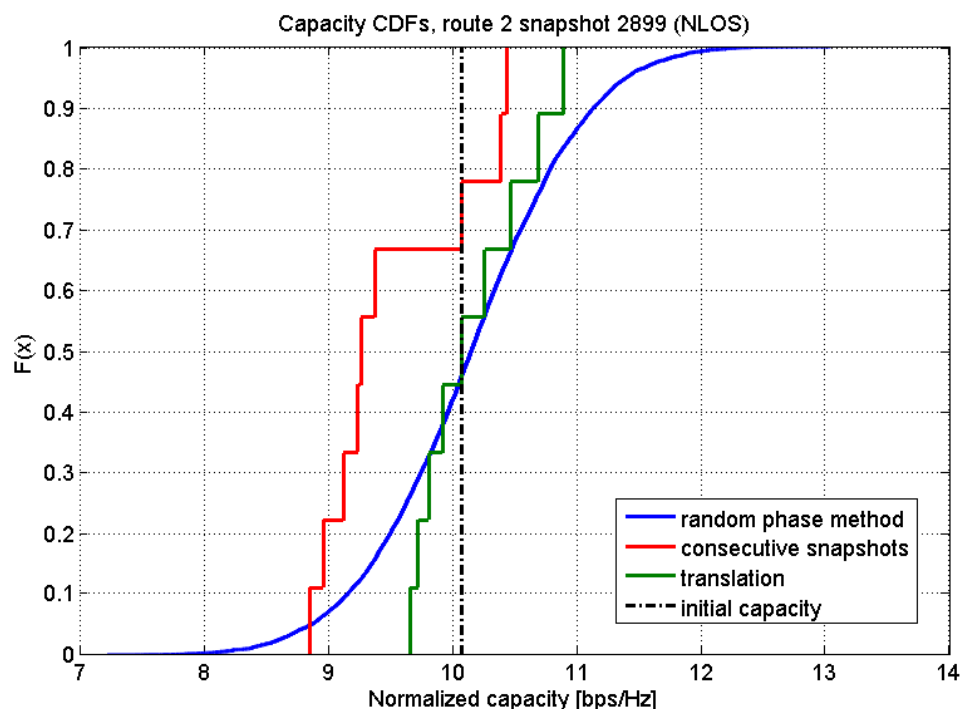


FIG. 5.6: Capacity CDFs derived from different methods

Capacity analysis: The route considered is LOS to NLOS route 2 (Figure 4.2): first 15 meters LOS and then 45 meters NLOS. An AGC (Automatic Gain Control) was supposed to be used; hence the SNR was settled, to 10 dB, which is a reasonable value. The effect of pathloss is thus neglected, thus the capacity is directly linked to the normalized correlation matrix $\widetilde{\mathbf{H}}\widetilde{\mathbf{H}}^H$. The calculation was done for one snapshot per meter, which leads to 60 capacity CDFs. The capacity comparison between SAGE and ray tracing was based on the mean (ergodic) value obtained with the random phases method. The 10% or 90% outage capacities could also have been chosen, but they follow quite the same variations (Figure 5.7). The outage values can nonetheless be interesting to derive a coverage margin.

One concern was that ray tracing version used does not provide polarization information. It has nonetheless been sidestepped by “emulating” the polarization power matrix $[P_{VV} \ P_{VH}; P_{HV} \ P_{HH}]$. Two methods have been used:

First method: for all the measurement points considered, each relative polarization power level (of all the paths) was set to a constant value

Second method: for each measurement point considered, the relative polarization power levels (of all the paths) were set to the average value given by SAGE.

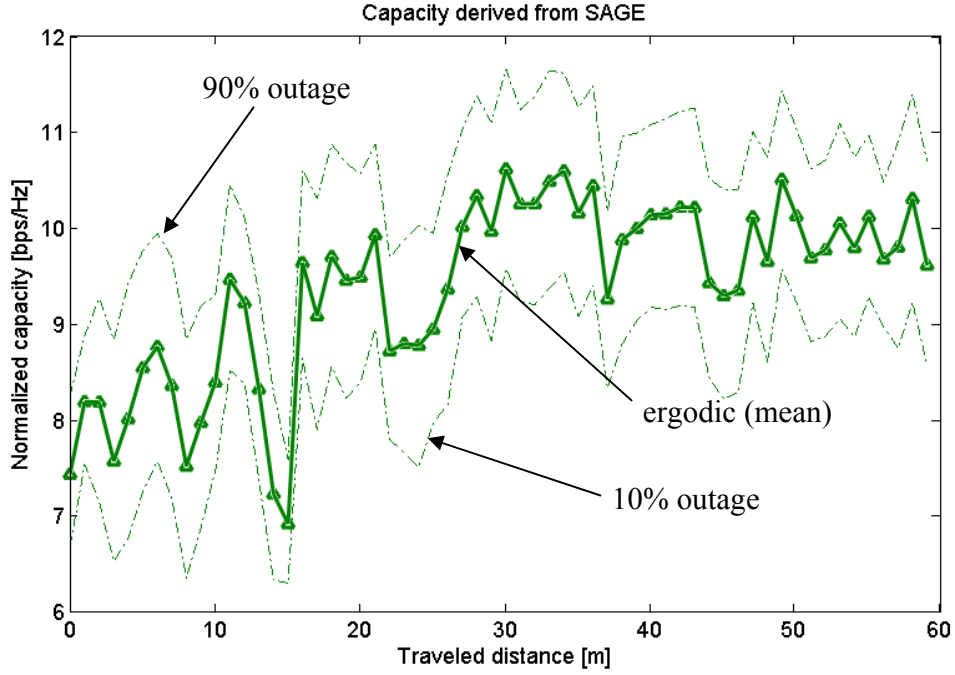


FIG. 5.7: Capacities derived from SAGE

Both methods do not consider the different polarizations of the different paths inside one snapshot. If the cross-polarization ratios (XPR) are introduced:

$$XPR_V = \frac{P_{VV}}{P_{VH}}, \quad (5.19)$$

$$XPR_H = \frac{P_{HH}}{P_{HV}}, \quad (5.20)$$

these two methods involve to fix the XPRs to a given value, either fixed or calculated from SAGE (Figure 5.8). The first method was first fixing the polarization powers to the following values, which correspond to the average values observed over the whole measurement campaign:

$$P_{VV} = P_{HH} + 3dB = P_{HV} + 10dB = P_{VH} + 10dB \quad (5.21)$$

which leads this way to:

$$XPR_V = 10dB, XPR_H = 7dB \quad (5.22)$$

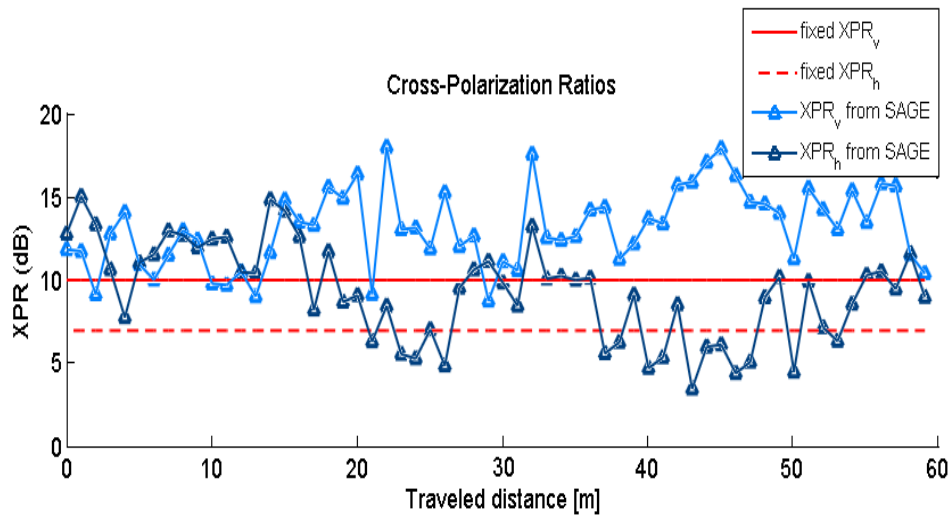


FIG. 5.8: XPRs on route 2

The 3 capacities (capacity derived from SAGE, capacity derived from ray tracing with fixed XPR and capacity derived from ray tracing with XPR from SAGE) are displayed in Figure 5.9. The global variations are similar: the capacity grows from NLOS to LOS as expected; rays are more correlated in LOS and close to LOS areas. The capacity increases in the 15 first NLOS meters, and it then tends to become stable. Statistically the differences are small (Table 5.1). On a smaller scale, SAGE and ray tracing do not always match: e.g. the opposite variations around 15 meters, and the exaggerated

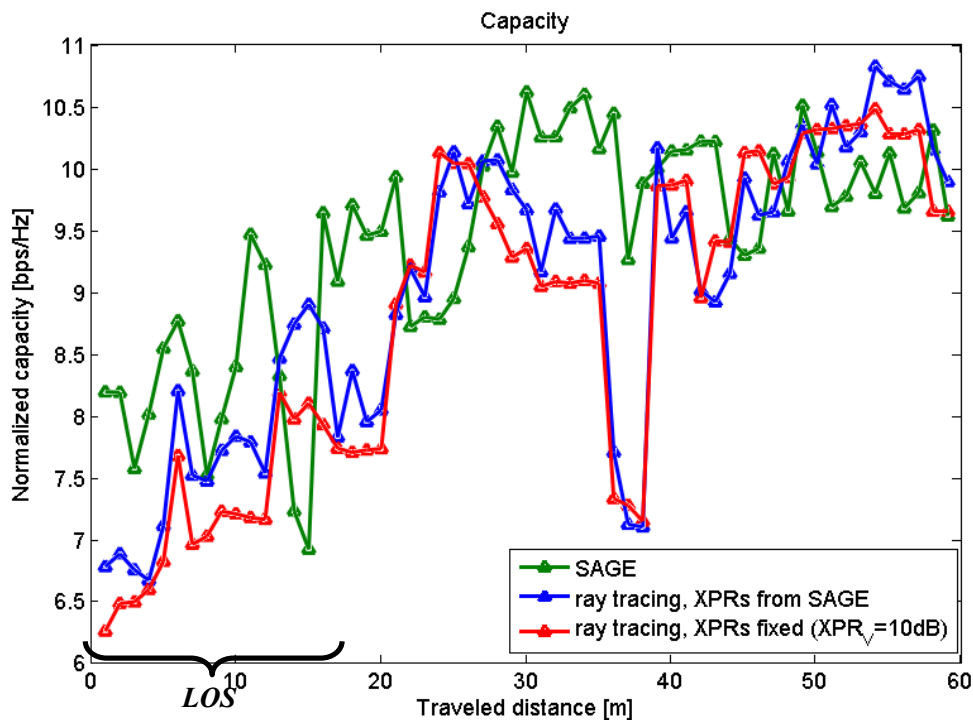


FIG. 5.9: Capacity comparison

decrease predicted by ray tracing around 38 m. But, once more, the capacity coverage does not require the precise small scale variations.

The two methods of “emulating” polarization provide close results, but some differences can nonetheless be noticed, especially in the zones where XPR_V and XPR_H from SAGE have close values (cf Figure 5.8; corresponds to LOS zone, around 30 meters and around 60 meters distance). The fixed XPRs method provides interesting results, as this method does not require any additional calculation or measurement and could thus be extended to zones with no measurement available.

The two methods, based on different polarization emulation, gave different results; hence the dependence of XPRs on capacity will now be investigated. To that end, the first method is repeated with different constant values, which also correspond better to SAGE average XPRs on the route 2 (see Figure 5.8):

$$XPR_V = 13dB, XPR_H = 10dB \text{ (and } P_{VV} = P_{HH} + 3dB), \quad (5.23)$$

The capacity obtained is displayed in Figure 5.10 together with previous results of the first method. The influence of XPR is clearly highlighted: capacity grows with XPRs, and a 3dB increase in XPRs here corresponds to an increase of 0.2 to 0.5 bps/Hz. This influence could be checked by a calculation on a simpler 2x2 MIMO system, with dual-polarized antenna arrays (see Annex A). One possible explanation is that the vertically polarized (VP) rays encountering cross-polarization interfere with the corresponding ray which was emitted with horizontal polarization (HP). Note in Table 5.1 that these new values as well provide better statistical results when compared to SAGE.

The aforementioned observation on XPR dependence is naturally inseparable from the system considered, e.g. if the transmitting antenna array was single-polarized and the receiving dual-polarized, then the capacity would probably grow as the XPR decreases.

It results from the comparison with SAGE that the capacity prediction from ray tracing is acceptable for capacity coverage purpose, especially with a fixed polarization and the values given in (5.23) (see Table 5.1 and Figures 5.9-5.10). Hence the capacity coverage derived by ray tracing can be studied. The zone studied is 1150x1050 m² wide (Figure 5.11). As the number of points considered is about 30,000 with a 5 m resolution grid, the

TABLE 5.1: Capacities derived from SAGE and RT: statistics

		mean difference	standard deviation
ray tracing, polarization:	from SAGE	0.41 bps/Hz	1.08 bps/Hz
	fixed (XPR_V=10dB)	0.62 bps/Hz	1.22 bps/Hz
	fixed (XPR_V=13dB)	0.28 bps/Hz	1.10 bps/Hz

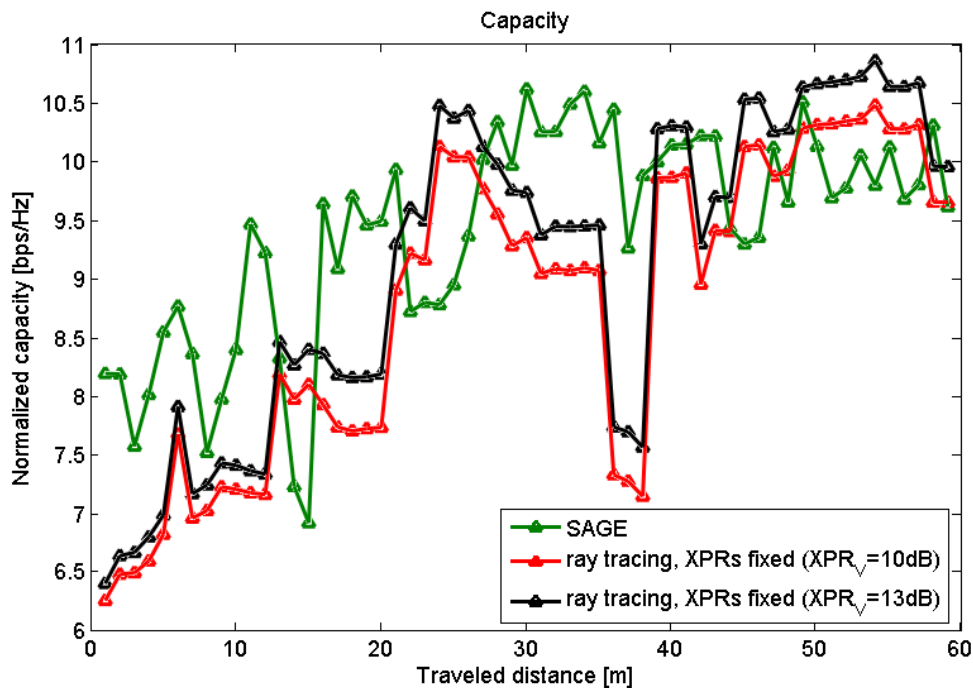


FIG. 5.10: Cross-polarization influence on ergodic capacity

number of occurrences for the random phases method was decreased from 10,000 to 64. One single capacity calculation then takes around 30 seconds of time instead of 1-2 hours, hence the total computation time is around 10 days. The accuracy of the prediction is of course also lower, thus the values should be cautiously interpreted. The changes from 16 (which was the number of occurrences originally chosen) to 64 occurrences have been studied on the coverage map; the differences were up to 1 bps/Hz.

The same system described previously, i.e. in particular SNR fixed to 10dB, is first considered. The capacity is derived for the whole zone grid from ray tracing, with constant values of XPRs from (5.23) (Figure 5.11). The capacity is globally about 8 bps/Hz, except:

- in LOS zones (and zones under the influence of those, e.g. the triangles drawn in Figure 5.11): the different paths are strongly correlated; the capacity is then around 6 bps/Hz;
- in parallel streets and in wide streets/spaces: capacity reaches up to 10-12 bps/Hz. The multipath components are strongly decorrelated, as the different paths experienced numerous interactions (edge diffractions, diffraction above rooftops, reflections).

These two types of zone can be also noticed when looking at the azimuth angular and delay spreads (Figure 5.12). The relation between angle spread and delay spread is nevertheless not really obvious in the perpendicular streets (south-north oriented). Even if the different rays are strongly uncorrelated (cf. Figure 5.11), they are possibly arriving in a small angle and delay range.

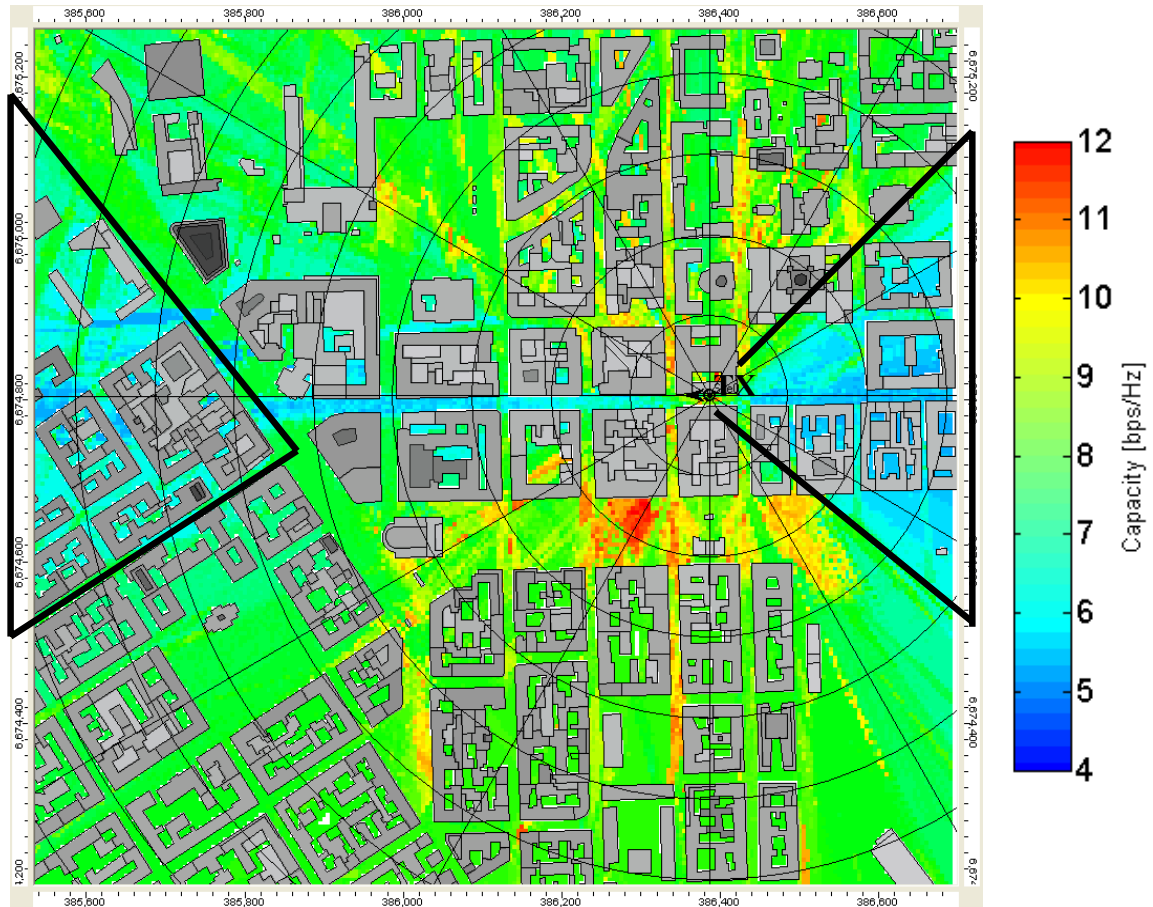


FIG. 5.11: Capacity coverage map, SNR=10 dB

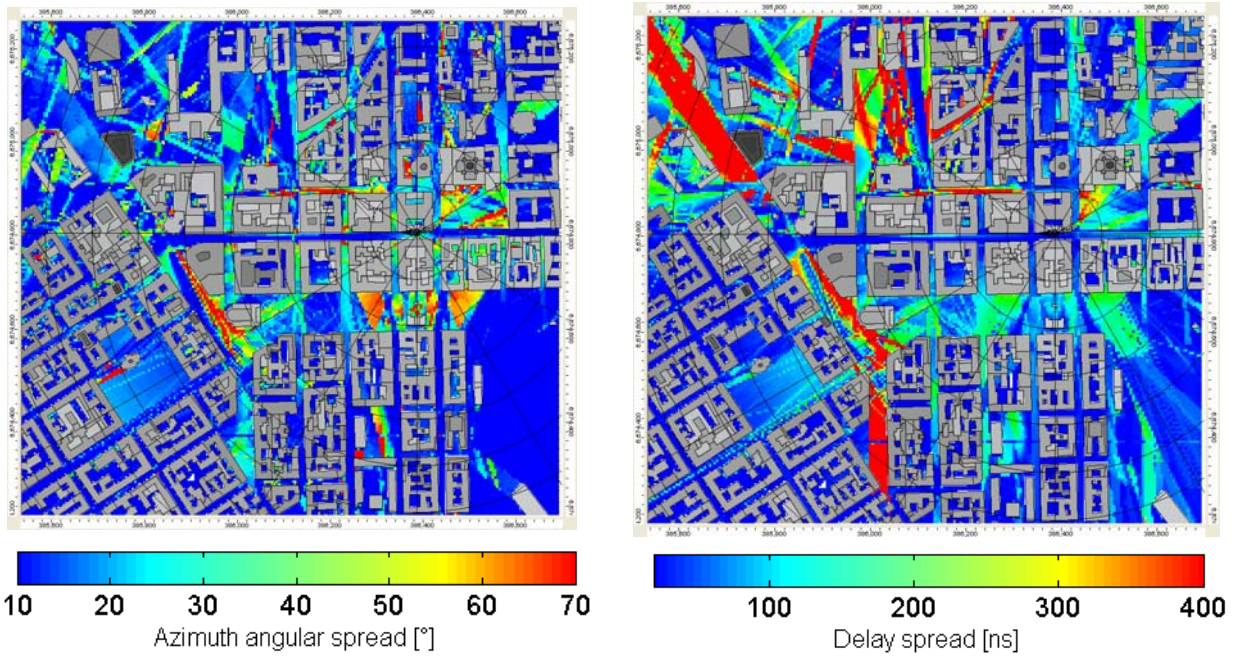


FIG. 5.12: Azimuth angular and delay spreads

Nonetheless, an unlimited AGC power, previously assumed by fixing the SNR, is not realistic. The capacity was thus derived once more, supposing the AGC is limited to ± 30 dB. The SNR was then computed considering a -130 dBm noise level (corresponds to a high-quality receiver), a desired SNR of 10 dB, and total transmitting power of 1W. The pathloss is first studied to predict which zones will be affected (Figure 5.13); actually, they correspond to the points having a pathloss outside the $[-90$ dB, -150 dB] interval. Inside the mentioned interval, the capacity results will be the same as previously, outside it they will be increased (SNR higher than 10 dB) or decreased (SNR lower than 10 dB). This can be checked on the resulting coverage map (Figure 5.14): the zones where the pathloss is too low have now a capacity of 4 bps/Hz instead of 6-8 bps/Hz previously, and in the vicinity of the transmitter the capacity is 12 bps/Hz instead of 8 bps/Hz. An interesting observation, which wasn't visible previously, can be made; the capacity coverage is better toward the south than the north. Different reasons might explain this; the location of the transmitting antenna (against the northern wall, thus discriminating diffractions above rooftops toward the north against those toward the south), the streets going quickly uphill to the north, and downhill then uphill to the south (Figure 4.5), and the southern wide parallel street (Esplanadi) which acts as a "resonator" for paths decorrelation (enhancing the reflections) and thus capacity. Note that the geodata used in ray tracing didn't include the Esplanadi vegetation which might change the results.

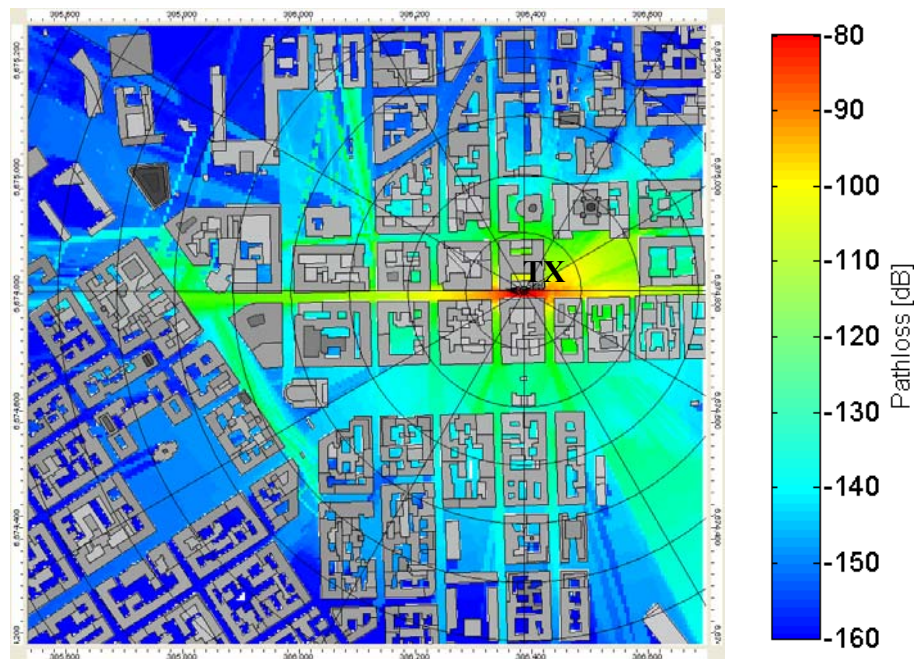


FIG. 5.13: Pathloss coverage

It is also interesting to compare the results to a SISO capacity coverage map (Figure 5.15). This map has been derived with channels 1 of the antennas presented previously (both channels are vertically polarized). First of all, capacity is lower; note that the legend

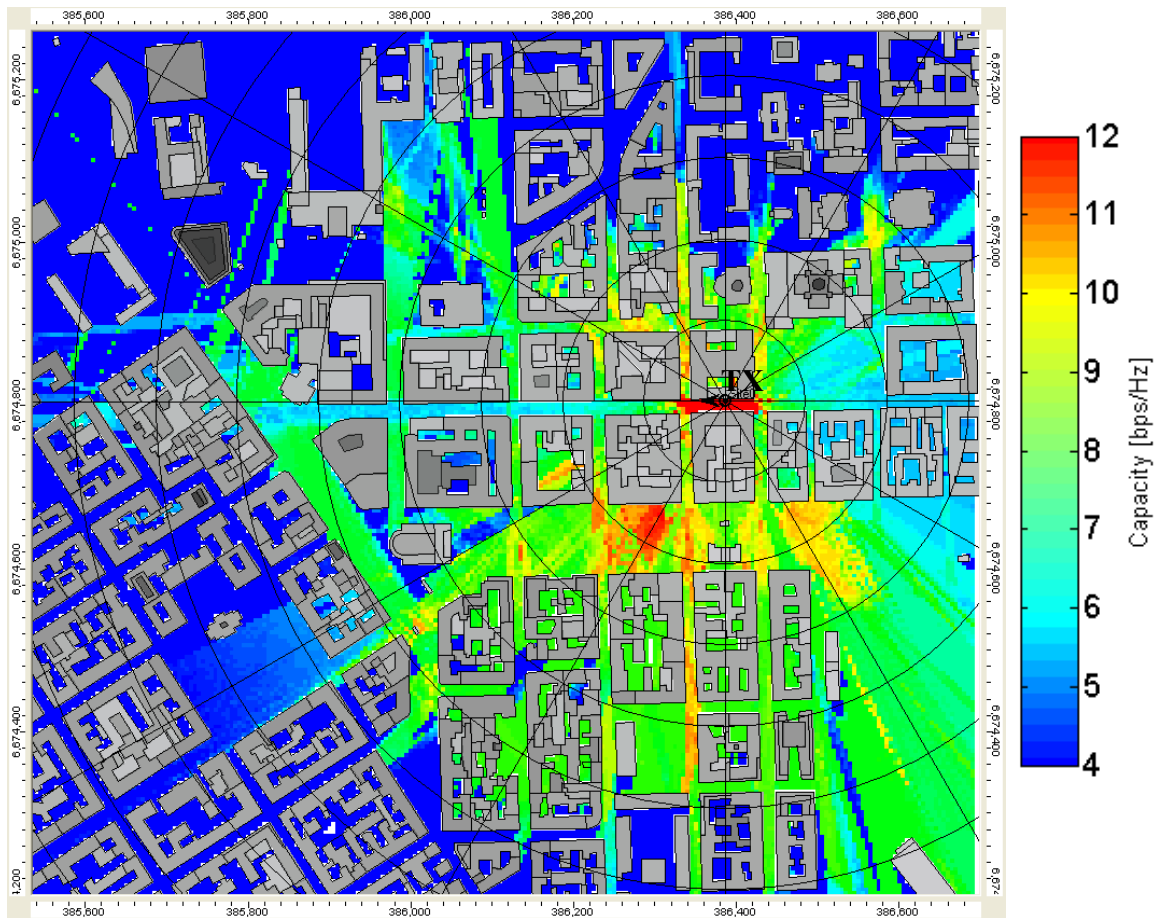


FIG. 5.14: Capacity coverage map, AGC limited to ± 30 dB

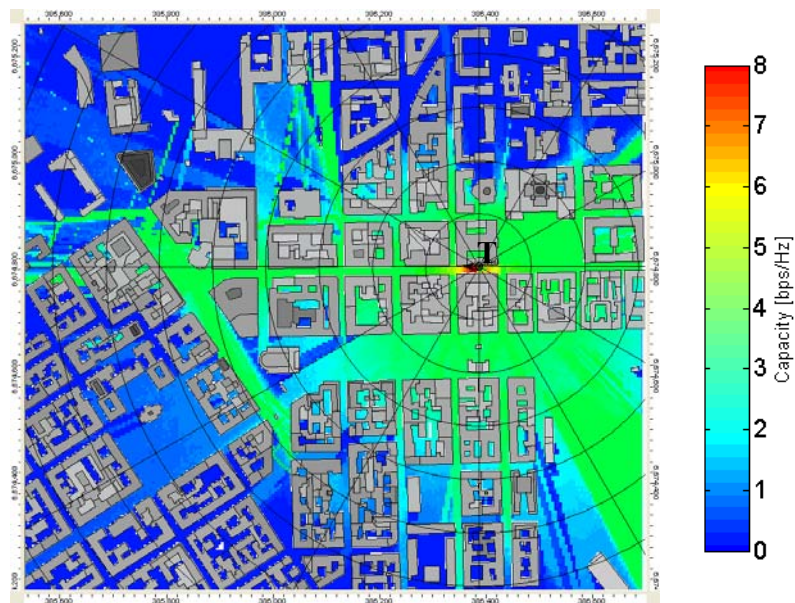


FIG. 5.15 SISO capacity coverage map, AGC limited to ± 30 dB

had thus to be changed to see the variations. A typical value of the SISO capacity on the map is 4 bps/Hz. Then, the only “high-capacity” zone is around the transmitter; unlike the MIMO coverage seen previously, no further zone is enhanced by multipath. With this antenna configuration, the capacity improvement from SISO to 4x4 MIMO is from 4 to 9 bps/Hz.

Supposing the derived capacity values to be reliable, cellular network planning can be started based on these results: cell size and reuse distance can be derived. For example, if considering a squared cell, for an ergodic MIMO capacity limit of 6 bps/Hz (corresponds to 120 Mbps for the 20 MHz bandwidth of 4G LTE –Long Term Evolution), the cell size would be about 650x650 m² (200 meters to the north, 450 meters to the south, 200 meters to the east, 450 meters to the west: see Figure 5.16).

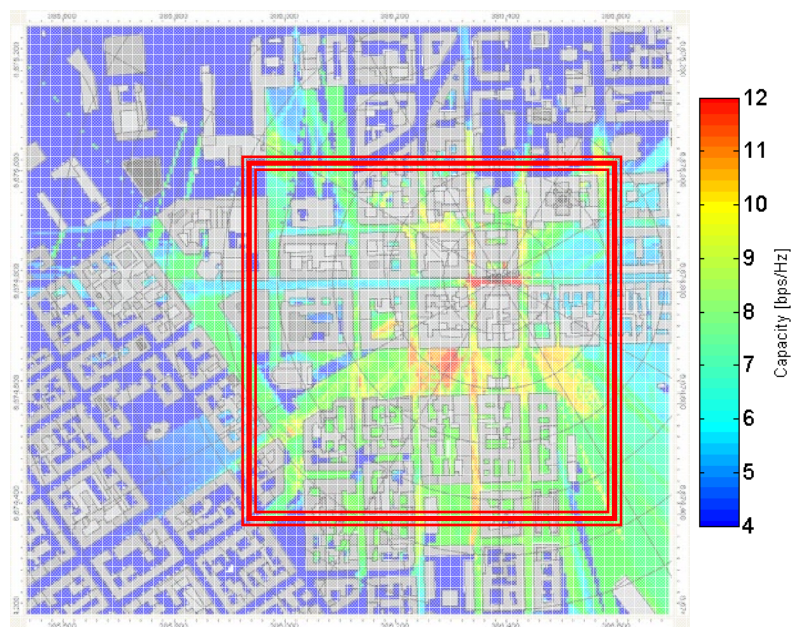


FIG. 5.16: Possible squared cell associated to the transmitter considered

VI – Conclusion

The goal of the thesis was to test the validity of Siradel's ray tracing software for predicting MIMO capacity coverage. Thanks to the developed analysis tools, a comparison with the measurements was carried out. This simulation appeared to be reliable enough to compute capacity, and a large capacity coverage map was finally provided.

First the path correlation indicators, which are delay spread and azimuth angular spread, and then capacity itself, were compared to measurement results. As the deterministic propagation models have been derived for a general behavior of large zones, and this study concentrates on a really small scale (microcell case with a distance Tx-Rx between 75 and 170 meters), some differences between simulations and measurements were expected. However, the observed differences were sufficiently small not to affect the capacity calculation significantly. Without the SNR influence the capacity comparison was actually satisfactory on a large scale. As pathloss prediction with ray tracing and thus SNR has been shown to be reliable, the used ray tracing tool could then properly predict the capacity of the channel for the large scale variations, hence for capacity coverage.

Eventually, a capacity map of the measurement neighborhood could then be produced based on the simulation from Siradel Volcano ray tracing software. A 650x650 m² area around the transmitter, with a minimum capacity of 6 bps/Hz corresponding to the very high data rates of fixed networks, could then be inferred. This map allows deriving capacity coverage of the studied cell, and thus this method, once confirmed to be reliable, could be used for cellular network planning.

A few continuation possibilities: The uncertainties of ray tracing-based predictions should be thoroughly analyzed to validate the method used. Other measurement campaigns could be also used in that end. The prediction of multipath components and capacity might as well be improved by e.g. taking into account the influence of non-UTD phenomena (diffuse scattering). In addition, the influence of cross-polarization on capacity dependence could be further investigated, together with the XPR variation (especially XPR_V variations). More sophisticated super-resolution algorithms, like EKF (Extended Kalman Filter) and RIMAX, could also be used to confirm the comparisons made.

Annex A: Polarization influence on capacity

A 2x2 dual-polarized MIMO system is considered, with the following channel matrix:

$$H = \begin{bmatrix} h_{HH} & h_{HV} \\ h_{VH} & h_{VV} \end{bmatrix} \quad (7.1)$$

The influence of XPR on capacity is studied for this particular system. Some simple XPR-extreme cases and their respective capacity calculated from (5.15) can first be studied:

$$\begin{aligned} \text{(i)} \quad H &= \begin{bmatrix} 1 & 1 \\ 1 & 1 \end{bmatrix} \quad (\Rightarrow XPR_V = XPR_H = 0) \\ &\Rightarrow C = \log_2(1+2\rho) \end{aligned} \quad (7.2)$$

$$\begin{aligned} \text{(ii)} \quad H &= \begin{bmatrix} 0 & 1 \\ 1 & 0 \end{bmatrix} \quad (\Rightarrow XPR_V = XPR_H = -\infty) \\ &\Rightarrow C = \log_2(1+2\rho+\rho^2) \end{aligned} \quad (7.3)$$

$$\begin{aligned} \text{(iii)} \quad H &= \begin{bmatrix} 1 & 0 \\ 0 & 1 \end{bmatrix} \quad (\Rightarrow XPR_V = XPR_H = +\infty) \\ &\Rightarrow C = \log_2(1+2\rho+\rho^2) \end{aligned} \quad (7.4)$$

These extreme cases seem to support that capacity grows together with XPRs absolute values.

The general case is now studied. If we nonetheless suppose that:

$$|h_{HH}|^2 + |h_{HV}|^2 = |h_{VV}|^2 + |h_{VH}|^2 = P_h/2, \quad (7.5)$$

where $P_h = \|\mathbf{H}\|_F$, it can be deduced from (5.11) that:

$$C = E_H \left\{ \log_2 \begin{vmatrix} 1 + \frac{P_0 P_h}{4\sigma_N^2} & \xi^* \\ \xi & 1 + \frac{P_0 P_h}{4\sigma_N^2} \end{vmatrix} \right\} \quad (7.6)$$

$$= E_H \left\{ \log_2 \left(\left(1 + \frac{P_0 P_h}{4\sigma_N^2} \right)^2 - |\xi|^2 \right) \right\}, \quad (7.7)$$

where $\xi = \frac{P_0}{2\sigma_N^2} (h_{HH} h_{VH}^* + h_{HV} h_{VV}^*)$. If the XPRs are artificially increased by lessening the two cross-polarizations as follows:

$$h_{VH}' = h_{VH}/\gamma \text{ and } h_{HV}' = h_{HV}/\gamma, \quad (7.8)$$

where h_{VH}' and h_{HV}' are the new components of the matrix and $\gamma > 1$, the related ξ' and P_h' can be written as follows:

$$|\xi'|^2 = \frac{|\xi|^2}{\gamma^2} \quad (7.9)$$

$$P_h' = |h_{HH}|^2 + |h_{VV}|^2 + \frac{|h_{HV}|^2 + |h_{VH}|^2}{\gamma^2} \quad (7.10)$$

And the corresponding capacity is then:

$$\mathcal{C}' = E_H \left\{ \log_2 \left(\left(1 + \frac{P_0 P_h'}{4\sigma_N^2} \right)^2 - |\xi'|^2 \right) \right\} \quad (7.11)$$

$$= E_H \left\{ \log_2 \left(\left[\left(1 + \frac{P_0 P_h}{4\sigma_N^2} \right)^2 - |\xi|^2 \right] + \beta \right) \right\}, \quad (7.12)$$

with

$$\beta = \left(1 - \frac{1}{\gamma^2} \right) \left(\frac{P_0}{4\sigma_N^2} \right)^2 \left(4|\xi|^2 + \left(1 - \frac{1}{\gamma^2} \right) (|h_{HV}|^2 + |h_{VH}|^2)^2 - 2 \left(\frac{4\sigma_N^2}{P_0} + P_h \right) (|h_{HV}|^2 + |h_{VH}|^2) \right) \quad (7.13)$$

If $|h_{HV}|^2, |h_{VH}|^2 \ll |h_{HH}|^2, |h_{VV}|^2$, which corresponds to $XPR_V, XPR_H \gg 1$, then $\beta > 0$, and thus:

$$\mathcal{C}' > \mathcal{C} \quad (7.14)$$

In conclusion, with the considered system, it has been showed that capacity increases together with the XPRs if $XPR_V, XPR_H \gg 1$ (and symmetrically, capacity decreases together with XPRs if $XPR_V, XPR_H \ll 1$). This result should also be extended to similar dual-polarized MIMO system, as the 4x4 system of the present thesis.

References

- [1] L. C. Godara, "Application of Antenna Arrays to Mobile Communications, Part II: Beam-Forming and Direction-of-Arrival Considerations", *Proceedings of the IEEE*, vol. 85, no 8, pp. 1195-1245, Aug. 1997.
- [2] B.H. Fleury, M. Tschudin, R. Heddergott, D. Dahlhaus, K. Ingeman Pedersen "Channel parameter estimation in mobile radio environments using the SAGE algorithm" *IEEE Journal on Selected Areas in Communications*, vol. 17, no 3, pp. 434-450, March 1999.
- [3] J. Salmi, *Statistical Modeling and Tracking of the Dynamic Behavior of Radio Channels*, M.Sc. thesis, Helsinki University of Technology, Finland, June 2005.
- [4] T. S. Rappaport, *Wireless Communications, Principles and Practice*, Prentice Hall, Upper Saddle River, 641 p., 1996.
- [5] L. M. Correia, *Mobile Broadband Multimedia Networks: Techniques, Models and Tools for 4G*, Academic Press, 600 p., 2006.
- [6] ETSI Technical Report, Universal Mobile Telecommunications System (UMTS); *Spatial channel model for Multiple Input Multiple Output (MIMO) simulations* (3GPP TR 25.996 version 6.1.0 Release 6) on <http://www.3gpp.org> (last checked 14.08.2008).
- [7] www.ist-winner.org (last checked 14.08.2008).
- [8] M. Hata, "Empirical formula for propagation loss in land mobile radio services", *IEEE Transactions on Vehicular Technology*, vol. 29, no 3, pp. 317-325, Aug 1980.
- [9] E. Damosso and L. Correia, *Digital Mobile Radio Towards Future Generation Systems, COST 231 Final Report*, European Commission, 474 p., 1999.
- [10] F. Ikegami, T. Takeuchi, and S. Yoshida, "Theoretical prediction of mean field strength for urban mobile radio", *IEEE Transactions on Antennas and Propagation*, vol. 39, no.3, pp. 299-302, March 1991.
- [11] J. Walfisch, H.L. Bertoni, "A theoretical model of UHF propagation in urban environments", *IEEE Transactions on Antennas and Propagation*, vol. 36, no 12, pp. 1788-1796, Dec. 1988.
- [12] R.G. Kouyoumjian, P.H. Pathak, "A uniform geometrical theory of diffraction for an edge in a perfectly conducting surface", *Proceedings of the IEEE*, vol. 62, no 11, pp. 1448-1461, Nov. 1974.

- [13] Y. Corre, Y. Lostanlen, Y. Le Helloco, "A new approach for radio propagation modeling in urban environment: knife-edge diffraction combined with 2D ray-tracing", *IEEE 55th Vehicular Technology Conference*, vol. 1, pp. 507-511, 6-9 May 2002 .
- [14] Y. Corre, Y. Lostanlen, "3D urban propagation model for large ray-tracing computation", *International Conference on Electromagnetics in Advanced Applications*, pp. 399-402, 17-21 Sept. 2007.
- [15] J.-P. Rossi, Y. Gabillet, "A mixed ray launching/tracing method for full 3-D UHF propagation modeling and comparison with wide-band measurements", *IEEE Transactions on Antennas and Propagation*, vol. 50, no 4, pp. 517-523, Apr 2002.
- [16] J. Deygout, "Multiple knife-edge diffraction of microwaves", *IEEE Transactions on Antennas and Propagation*, vol. 14, no 4, pp. 480- 489, Jul 1966.
- [17] J.D. Parsons, D.A. Demery, A.M.D. Turkmani, "Sounding techniques for wideband mobile radio channels: a review", *IEEE Proceedings I in Communications, Speech and Vision*, vol. 138, no 5, pp. 437-446, Oct 1991.
- [18] W.R. Young Jr., L.Y. Lacy, "Echoes in Transmission at 450 Megacycles from Land-to-Car Radio Units", *Proceedings of the IRE*, vol. 38, no 3, pp. 255-258, March 1950.
- [19] R. J. Pirkel, *A sliding correlator channel sounder for ultra-wideband measurements*, M.Sc. thesis, Georgia Institute of Technology, U.S., August 2007.
- [20] D. C. Cox, "Delay Doppler Characteristics of Multipath Propagation at 910 MHz in a Suburban Mobile Radio Environment", *IEEE Transactions on Antennas and Propagation*, vol.: 20, no 5, pp. 625-635, Sep. 1972.
- [21] J. Kivinen, *Development of wideband radio channel measurement and modeling techniques*, D.Sc. dissertation, Helsinki University of Helsinki, Finland, March 2001.
- [22] V.-M. Kolmonen, J. Kivinen, L. Vuokko, P. Vainikainen, "5GHz MIMO Radio Channel Sounder", *IEEE Transactions on Instrumentation and Measurement*, vol. 55, no 4, pp. 1263-1269, Aug. 2006.
- [23] J. Fessler and A. Hero, "Space-Alternating Generalized Expectation-Maximization Algorithm", *IEEE Transactions on Signal Processing*, vol. 42, no 10, pp. 2664-2677, Oct. 1994.
- [24] B. Fleury, P. Jourdan, A. Stucki, "High-Resolution Channel Parameter Estimation for MIMO Applications Using the SAGE Algorithm", *International Zurich Seminar on Broadband Communications, Access, Transmission, Networking*, pp. 30-1 - 30-9, 2002.

- [25] B. H. Fleury, "First- and Second-Order Characterization of Direction Dispersion and Space Selectivity in the Radio Channel" *IEEE Transactions on Information Theory*, vol. 46, no 6, pp. 2027-2044, Sep. 2000.
- [26] T. M. Cover, J. A. Thomas, *Elements of Information Theory*, John Wiley & Sons, Inc., 542p., 1991.
- [27] B. Holter, "On the Capacity of the MIMO Channel – A Tutorial Introduction", Norwegian University of Science and Technology, http://www.iet.ntnu.no/projects/beats/Documents/MIMO_introduction.pdf (last checked 14.08.2008).
- [28] E. Telatar, "Capacity of Multi-antenna Gaussian Channels", *European Transactions on Telecommunications (ETT)*, vol. 10, no. 6, pp. 585-596, 1999.
- [29] A. A. Abouda, *Characterization of MIMO Channel Capacity in Urban Microcellular Environment*, D.Sc. dissertation, Helsinki University of Technology, Finland, April 2007.
- [30] G. J. Foschini and M. J. Gans, "On Limits of Wireless Communications in a Fading Environment when Using Multiple Antennas", *Wireless Personal Communications*, vol. 6, pp. 311-335, 1998.
- [31] P. Suvikunnas, J. Villanen, K. Sulonen, C. Icheln, J. Ollikainen, and P. Vainikainen, "Evaluation of the performance of multiantenna terminals using a new approach", *IEEE Transactions on Instrumentation and Measurement*, vol. 55, no 5, pp. 1804-1813, Oct. 2006.
- [32] J. Villanen, P. Suvikunnas, C. Icheln, J. Ollikainen, P. Vainikainen, "Performance Analysis and Design Aspects of Mobile-Terminal Multiantenna Configurations", *IEEE Transactions on Vehicular Technology*, vol. 57, no 3, pp. 1664-1674, May 2008.
- [33] Andreas F. Molisch, Martin Steinbauer, Martin Toeltsch, Ernst Bonek, Reiner S. Thomä, "Capacity of MIMO Systems Based on Measured Wireless Channels", *IEEE Journal on selected Areas in Communications*, vol. 20, no 3, pp. 561-569, Apr. 2002
- [34] W.C. Jakes, "Microwave Mobile Communications", Wiley-IEEE Press, 656 p., 1994.